Reduced order variational multiscale enrichment method for elasto-viscoplastic problems

Shuhai Zhang[*] and Caglar Oskay[†]

Department of Civil and Environmental Engineering
Vanderbilt University
Nashville, TN 37235

Abstract

This manuscript presents the formulation and implementation of a novel reduced order variational multiscale enrichment (ROVME) method for elasto-viscoplastic problems. This method provides a hierarchical model order reduction technique based on the eigenstrain concept to approximate the fine scale response resolved at subdomains of interest. By eliminating the requirement of direct fine scale discretization, the computational effort associated with the variational multiscale enrichment (VME) method is significantly reduced. The model order reduction is achieved in the scale-coupled inelastic problem by automatically satisfying the microscale equilibrium state through the eigenstrain concept and coarse discretization of inelastic strain fields within the microscale domain. The inelastic material behavior is idealized with coupled Perzyna type viscoplasticity and flow stress evolution based on the Johnson-Cook model. Numerical verifications are performed to assess the capabilities of the proposed methodology, against the direct VME method with detailed fine scale resolutions. The verification results demonstrate high accuracy and computational efficiency of the reduced order VME framework for elasto-viscoplastic problems with material heterogeneity.

Keywords: Multiscale modeling; Variational multiscale enrichment; Reduced order modeling; Elasto-viscoplastic; Eigenstrain-based modeling.

---

[*]Department of Civil and Environmental Engineering, Vanderbilt University, Nashville, TN 37235, United States. Email: shuhai.zhang@vanderbilt.edu

[†]Corresponding author address: VU Station B#351831, 2301 Vanderbilt Place, Nashville, TN 37235. Email: caglar.oskay@vanderbilt.edu

1 Introduction

We are concerned with efficiently evaluating mechanics problems with global-local character. Global-local refers to a class of problems, in which it is necessary to capture the detailed fine scale behavior at small subdomains of the problem. Typically the response within the remainder of the domain is of secondary importance and approximated using coarse discretization or coarse scale modeling. A number of computational methods have been proposed including the global-local finite element method [38, 40, 31, 13, 18], the S-version finite element method [12], the domain decomposition method [30], the generalized finite element method [9, 21], multiscale coupling based on Lagrange multiplier method [32], among others. These approaches permit the incorporation of additional geometric features such as crack tips [12, 9, 21], as well as material heterogeneities [30] at local subdomains with accurately captured load fields and response mechanisms. However, for many problems, the computational complexity associated with resolving the local features even for small subdomains could be prohibitive, notwithstanding a few examples based on very high performance computing [35].

A number of recent multiscale computational methods are also well suited to address problems that exhibit global-local character. Particularly the multiscale methods which permit the evaluation of scale inseparable problems such as multiscale finite element method [22, 11], multiscale aggregating discontinuities [5, 47], numerical subgrid upscaling [2, 3], variational multiscale enrichment [41, 42, 51] among others have been shown to successfully address global-local problems. The common idea behind these approaches is the additive split of the principal response fields into macro (or coarse) and micro (or fine) components with equal order of magnitude (in contrast to scale separable models, where the fine component is considered a perturbation to the coarse component [4, 20, 17, 48]). The coarse component of the response is evaluated using a coarse grid whereas the fine scale response is evaluated using a fine grid resolving the features of the small scales. Similar to earlier global-local methods, the computational cost of these approaches are large enough to prohibit evaluation of realistic problems.

Variational multiscale method (VMM) originally proposed by Hughes et al. [23] allows the infusion of a fine scale response in an otherwise coarse representation. In contrast to the above mentioned approaches, the fine scale response is either evaluated analytically or semi-analytically through variational projection [25, 26]. The projection based approach eliminates the need to resolve the fine scale behavior, hence providing a tremendous computational efficiency. Garikipati and Hughes [15, 16] employed the analytical fine scale Green's operator for strain localization problems. Hughes and Sangalli [24] further optimized the projection operator for advection-diffusion problems. Masud and Xia [33] developed a stabilized VMM based on variational projection for small strain inelasticity. Masud and Truster [34] extended

the stabilized VMM for nearly incompressible elasticity. Arbogast [2, 3], Juanes and Dub [27] performed the projection through numerical Green's functions to solve porous media flow problems. To the best of the authors' knowledge, the projection approach has not been employed to address complex response mechanisms induced by material heterogeneities at the fine scale. The variational multiscale enrichment [41, 42, 51] method, a variant of the numerical subgrid algorithm, has been recently proposed to study problems with fine scale material heterogeneity. This approach relies on the resolution of the fine scale problems which is computationally expensive for simulation of large scale systems.

In the current manuscript, we provide an alternative reduced order modeling approach in the context of variational multiscale enrichment method to address global-local problems. The proposed model order reduction approach is based on the concepts of transformation field analysis pioneered by Dvorak and coworkers [10]. The main idea is to express the response field as a function of influence functions and coefficient tensors that are computed at the preprocessing stage prior to a structural analysis. The influence functions ensure that the microstructural equilibrium is a-priori satisfied for arbitrary states of deformation. While this approach has been previously applied in the context of computational homogenization [39, 43, 8], it has not been previously formulated for scale inseparable multiscale methods, to the best of the authors' knowledge. This manuscript presents the reduced order variational multiscale enrichment (ROVME) formulation for heterogeneous materials that exhibit elasto-viscoplastic behavior. The implementation procedure and numerical approaches employed are described. The proposed ROVME approach is thoroughly verified against the direct variational multiscale enrichment (VME) method [51]. The proposed approach is able to capture the local and global response mechanisms with reasonable accuracy at the fraction of the cost.

This manuscript provides the following novel contributions: (1) The eigenstrain-based reduced order modeling approach is extended to scale inseparable problems; (2) The local problem within the VME framework is evaluated based on a much reduced approximation basis without significant loss in accuracy; and (3) The ROVME approach provides the ability to control efficiency/accuracy characteristics since the model order is controlled within the reduced order modeling framework.

The remainder of this manuscript is organized as follows: Section 2 provides the problem statement and governing equations of the VME method. Section 3 details the reduced order VME formulation for inelastic mechanical problems with elasto-viscoplastic material behavior. Section 4 illustrates the implementation strategy of the ROVME methodology. Section 5 presents the numerical verification studies including global-local response and assessment of computation efficiency. Section 6 provides the conclusions and future research directions.
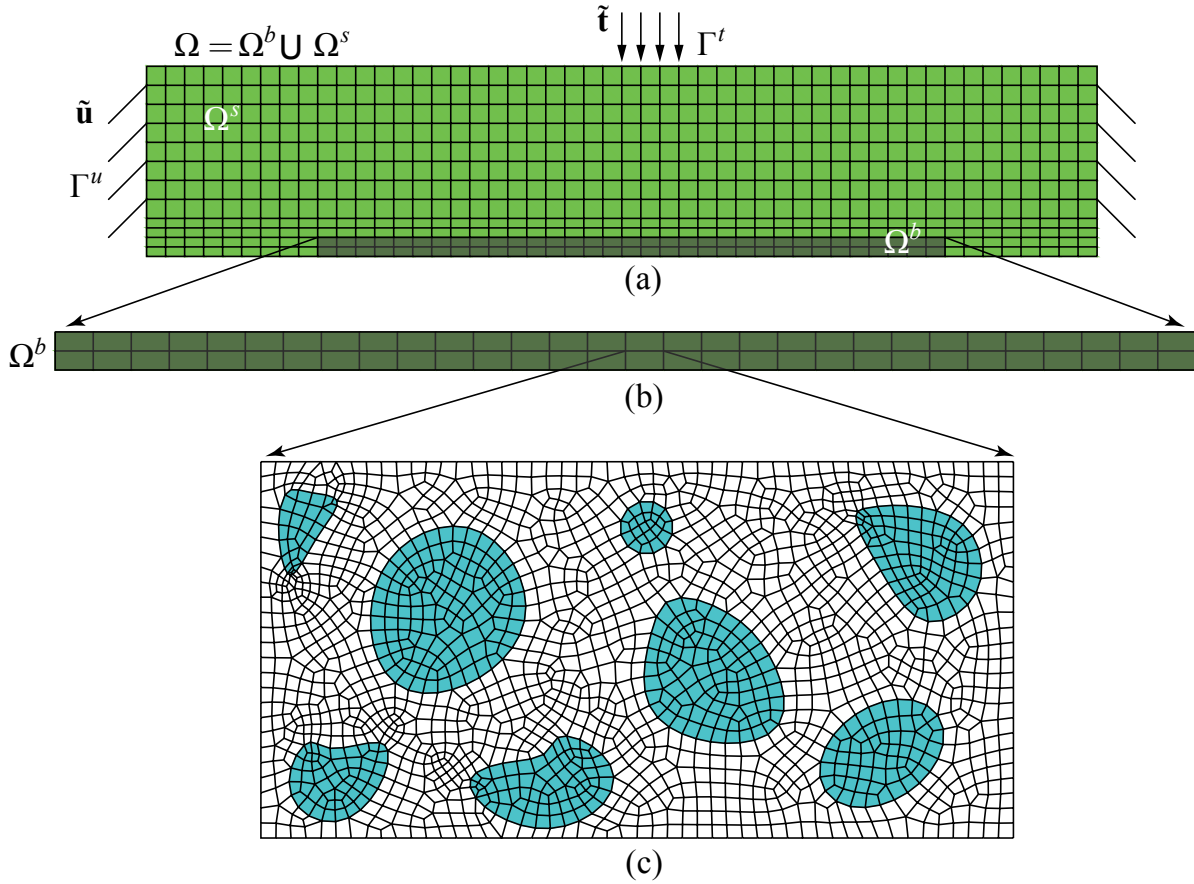
Figure 1: The schematic representation of: (a) the overall problem domain; (b) the enrichment region; (c) an enrichment domain with full discretization.

2   Variational Multiscale Enrichment

We start by setting up the governing equations of the direct variational multiscale enrichment (VME) method, which serves as the starting point for the proposed model order reduction approach. Within the problem domain, the material is taken to behave elasto-viscoplastically. The setting of the problem formulation for the variational multiscale enrichment of viscoplastic materials have been discussed in detail in Ref. [51]. Since the proposed reduced order model also relies on it, we provide a review of the problem setting below. The domain of the structure is denoted as $\Omega \subset \mathbb{R}^{n_{\mathrm{sd}}}$ (Fig. 1) where n_{sd} is the number of spatial dimensions. The equilibrium equation is expressed as:

$$\nabla \cdot \boldsymbol{\sigma}(\mathbf{x}, t) = 0; \quad \mathbf{x} \in \Omega, \quad t \in [0, t_o] \tag{1}$$

where, $\mathbf{x}$ and t are the position and time coordinates, respectively; $\boldsymbol{\sigma}$ is the stress tensor; ∇ is the gradient operator; $(\cdot)$ is the inner product; and t_o is the end of the observation period.

The body force term could be incorporated into the formulation without significant difficulty. In the context of the applications considered in the study, the body force is often negligible compared with the external loads. In other applications such as of thin films or soft materials, the effect of the body force may be non-trivial. The time variability of the response fields stems from the quasi-static (as opposed to static) behavior induced by the presence of the viscous term in the constitutive behavior. That is the rate of loading affects constitutive response, making the problem time-dependent. The constitutive equation is expressed in the rate form as:

$$\dot{\boldsymbol{\sigma}}(\mathbf{x},t) = \mathbf{L}(\mathbf{x},t) : [\dot{\boldsymbol{\varepsilon}}(\mathbf{x},t) - \dot{\boldsymbol{\varepsilon}}^{vp}(\mathbf{x},t)] \tag{2}$$

in which, $\mathbf{L}$ is the tensor of elastic moduli; $\boldsymbol{\varepsilon}$ and $\boldsymbol{\varepsilon}^{vp}$ denote total strain and viscoplastic strain tensors, respectively. The superposed dot indicates material time derivative and (:) the double inner product. The boundary conditions are given as:

$$\text{Dirichlet B.C.:} \quad \mathbf{u}(\mathbf{x},t) = \tilde{\mathbf{u}}(\mathbf{x},t); \qquad \mathbf{x} \in \Gamma^u \tag{3}$$

$$\text{Neumann B.C.:} \quad \boldsymbol{\sigma}(\mathbf{x},t) \cdot \mathbf{n} = \tilde{\mathbf{t}}(\mathbf{x},t); \qquad \mathbf{x} \in \Gamma^t \tag{4}$$

where, $\tilde{\mathbf{u}}$ is the prescribed displacement along the Dirichlet boundary, Γ^u; $\tilde{\mathbf{t}}$ is the prescribed traction along the Neumann boundary, Γ^t. The external boundary is decomposed such that $\partial\Omega = \Gamma = \Gamma^u \cup \Gamma^t$ and $\Gamma^u \cap \Gamma^t \equiv \emptyset$.

The problem domain, Ω, is decomposed into two non-overlapping subregions, as illustrated in Fig. 1:

$$\Omega = \Omega_s \cup \Omega_b; \quad \Omega_s \cap \Omega_b \equiv \emptyset \tag{5}$$

where, Ω_b is the enrichment region and Ω_s is the substrate region. In the enrichment region, the microstructural heterogeneities are resolved. In the substrate region, a coarse scale representation of the homogenized microstructure is assumed to be sufficient for describing the mechanical response accurately. The enrichment region, Ω_b, is further discretized into a series of non-overlapping enrichment domains. The discretization is performed in a manner that each of the discretized enrichment domains can be represented by a single finite element at the coarse scale level, as illustrated in Fig. 1:

$$\Omega_b = \bigcup_{\alpha=1}^{n_{\text{en}}} \Omega_\alpha; \quad \Omega_\alpha \cap \Omega_\beta \equiv \emptyset \quad \text{when} \quad \alpha \neq \beta \tag{6}$$

where, n_{en} denotes the total number of enrichment domains in the structure. Within each enrichment domain, the microstructural heterogeneity is resolved and the local fine scale solution is numerically evaluated.

In the variational multiscale enrichment method, the displacement field is decomposed into

macroscale and microscale components through an additive two-scale decomposition:

$$\mathbf{u}(\mathbf{x}, t) = \mathbf{u}^M(\mathbf{x}, t) + \sum_{\alpha=1}^{n_{\text{en}}} \mathcal{H}(\Omega_\alpha)\mathbf{u}_\alpha^m(\mathbf{x}, t) \tag{7}$$

where, superscripts M and m denote the macroscale and microscale fields, respectively. The macroscale indicates the entire domain of the structure of interest (or when high gradients are present, the length scale of the process zone), whereas the microscale denotes the enrichment domain which resolves the microstructural heterogeneities. The concepts of the macro- and microscales are identical to those posited in scale separable theories (e.g. homogenization), the only difference being the characteristic size ratio is larger than zero. In the present formulation, the displacement field is resolved into macro- and micro- components through Eq. (7). The Heaviside function, $\mathcal{H}(\Omega_\alpha)$, is employed to ensure that the microscale displacement field, $\mathbf{u}_\alpha^m$, contributes to the displacement field only on the closure of the enrichment domain, Ω_α.

We seek to establish variational forms to evaluate the macroscale and microscale displacement fields. The macroscale response is sought such that $\mathbf{u}^M \in \mathcal{V}^M(\Omega)$, in which $\mathcal{V}^M(\Omega) \subset [H^1(\Omega)]^{n_{sd}}$ is the trial solution space for the macroscale. The microscale response within the enrichment domain, Ω_α, is determined such that $\mathbf{u}_\alpha^m \in \mathcal{V}_\alpha(\Omega_\alpha)$, in which $\mathcal{V}_\alpha(\Omega_\alpha) \subset [H^1(\Omega_\alpha)]^{n_{sd}}$ is the trial solution space for the microscale. For the uniqueness and stability of the decomposition shown in Eq. (7), linear independence of the macroscale and the microscale solution spaces is necessary [25, 15]. The solution space is the direct sum of the macroscale and microscale solution spaces [42]:

$$\mathcal{V}(\Omega) = \mathcal{V}^M(\Omega) \oplus \bigoplus_{\alpha=1}^{n_{\text{en}}} \mathcal{V}_\alpha(\Omega_\alpha) \tag{8}$$

Similar to the displacement field decomposition in Eq. (7), additive decomposition of the test function is performed as:

$$\mathbf{w} = \mathbf{w}^M + \sum_{\alpha=1}^{n_{\text{en}}} \mathcal{H}(\Omega_\alpha)\mathbf{w}_\alpha^m \tag{9}$$

where, $\mathbf{w}^M \in \mathcal{W}^M(\Omega) \subset [H_0^1(\Omega)]^{n_{\text{sd}}}$ is the macroscale test function and $\mathbf{w}_\alpha^m \in \mathcal{W}_\alpha(\Omega_\alpha) \subset [H^1(\Omega_\alpha)]^{n_{\text{sd}}}$ is the microscale test function of the enrichment domain, Ω_α. The test function space, $\mathcal{W}(\Omega)$, is decomposed using the additive sum as in Eq. (8).

In order to ensure the response field continuity along the inter-enrichment domain interfaces, the homogeneous Dirichlet boundary condition (residual-free bubble) is assumed along the microscale boundaries [6, 25]:

$$\mathbf{u}_\alpha^m(\mathbf{x}, t) = 0; \ \mathbf{x} \in \Gamma_\alpha \tag{10}$$

6

> **Remark 1.** In the context of direct VME, it is also possible to impose other boundary conditions (e.g., mixed boundary conditions proposed in Refs. [51, 42], periodic or Neumann boundary conditions) along the enrichment boundaries, some of which were demonstrated to provide better accuracy. The model order reduction is formulated using Dirichlet boundary conditions only. While the generalization to periodic boundary conditions is relatively straightforward, the model order reduction formulation using Neumann and mixed boundary conditions may include additional complications pertaining to the definition of time-invariant reduced order basis functions (influence functions) described in the next section.

Employing the two-scale decomposition of the displacement field and the test function, the macroscale equilibrium is obtained from Eq. (1) and the corresponding boundary conditions, by considering vanishing microscale test functions:

$$\int_{\Omega} \nabla \mathbf{w}^M : \boldsymbol{\sigma} \; d\Omega - \int_{\Gamma^t} \mathbf{w}^M \cdot \tilde{\mathbf{t}} \; d\Gamma = 0 \tag{11}$$

Similarly, the weak form of the microscale problem at an arbitrary enrichment domain, α, yields:

$$\int_{\Omega_{\alpha}} \nabla \mathbf{w}_{\alpha}^m : \boldsymbol{\sigma} \; d\Omega = 0; \quad \alpha = 1, 2, ... n_{\text{en}}. \tag{12}$$

The detailed formulation and mathematical constructs necessary to allow the multiscale decomposition is explained in Ref. [51] and skipped herein for brevity. Substituting the displacement decomposition (Eq. (7)) into Eq. (2), the stress-strain relationship is expressed as a function of the macro- and micro- variables in the rate form as:

$$\dot{\boldsymbol{\sigma}} = \mathbf{L} : \left[\dot{\boldsymbol{\varepsilon}}^M(\mathbf{u}^M) + \sum_{\alpha=1}^{n_{\text{en}}} \mathcal{H}(\Omega_{\alpha}) \; \dot{\boldsymbol{\varepsilon}}_{\alpha}^m(\mathbf{u}_{\alpha}^m) - \dot{\boldsymbol{\varepsilon}}^{vp}(\boldsymbol{\sigma}, \mathbf{u}^M, \mathbf{u}^m) \right] \tag{13}$$

While the proposed reduced order formulation can be extended to other forms of evolution equations, we employ a Perzyna-type viscoplasticity to describe the behavior of the material [51]. As illustrated in Fig. 1, the proposed modeling approach requires the evolution of the viscoplastic strain of $n_{\text{ph}} + 1$ materials, where n_{ph} denotes the number of phases within the microstructure. The additional material corresponds to the "homogenized" material defining the behavior within the substrate region, Ω_s. All materials are assumed to follow the same general constitutive form, with separate material parameter sets defining the behavior of each constituent. In the current study, the properties of the substrate material are obtained through the mixture theory. For more complex constitutive behavior, the homogenized macroscopic properties and the associated constitutive model forms can be obtained using the computational homogenization theory [14, 28, 52], based on sequential multiscale model-

ing [19], effective medium theories such as the linear comparison medium method [45], among others.

The rate effect of the presented quasi-static problem is time dependent which is characterized by the evolution of the viscoplastic strain as:

$$\dot{\boldsymbol{\varepsilon}}^{vp} = \gamma \left\langle \frac{f}{\sigma_y} \right\rangle^q \frac{\partial f}{\partial \boldsymbol{\sigma}} \tag{14}$$

where, γ is the fluidity parameter; σ_y the flow stress; q the viscoplastic hardening parameter; $\langle \cdot \rangle$ the Macaulay brackets (i.e., $\langle \cdot \rangle = ((\cdot) + |\cdot|)/2$); and f denotes the loading function which is defined using the classical J_2 plasticity:

$$f(\boldsymbol{\sigma}, \boldsymbol{\varepsilon}^{vp}) = \sqrt{3}\bar{\sigma} - \sigma_y(\bar{\varepsilon}^{vp}) \tag{15}$$

in which, $\bar{\sigma}$ is the second invariant of the deviatoric stress tensor, $\mathbf{s} = \boldsymbol{\sigma} - \mathrm{tr}(\boldsymbol{\sigma})\boldsymbol{\delta}/3$; $\mathrm{tr}(\cdot)$ the trace operator; $\boldsymbol{\delta}$ the Kronecker delta; and $\bar{\varepsilon}^{vp}$ denotes the effective viscoplastic strain defined as:

$$\bar{\varepsilon}^{vp} = \int_0^t \dot{\bar{\varepsilon}}^{vp} \, d\tau; \quad \dot{\bar{\varepsilon}}^{vp} = \sqrt{\frac{2}{3}\, \dot{\boldsymbol{\varepsilon}}^{vp} : \dot{\boldsymbol{\varepsilon}}^{vp}} \tag{16}$$

As a function of the effective viscoplastic strain, the flow stress is defined based on the Johnson-Cook model [44, 51]:

$$\sigma_y = A + B(\bar{\varepsilon}^{vp})^n \tag{17}$$

where, A, B and n are material parameters. Comparing with the standard Johnson-Cook model, the strain rate effect is modeled directly using the Perzyna formulation and the temperature dependence is suppressed for simplicity.

The macroscale and microscale response fields, along with their corresponding test functions, are discretized using the standard Bubnov-Galerkin approach. The finite element spaces are shown in the following:

$$\mathcal{V}^M(\Omega) \equiv \left\{ \mathbf{u}^M(\mathbf{x}, t) \middle| \mathbf{u}^M(\mathbf{x}, t) = \sum_{A=1}^{N_D} N_A(\mathbf{x}) \, \hat{\mathbf{u}}_A^M(t); \; \hat{\mathbf{u}}_A^M(t) = \hat{\mathbf{u}}^M(\mathbf{x}_A, t) \text{ if } \mathbf{x}_A \in \Gamma^u \right\} \tag{18}$$

$$\mathcal{V}_\alpha(\Omega_\alpha) \equiv \left\{ \mathbf{u}_\alpha^m(\mathbf{x}, t) \middle| \mathbf{u}_\alpha^m(\mathbf{x}, t) = \sum_{a=1}^{n_{d_\alpha}} n_{\alpha,a}(\mathbf{x}) \, \hat{\mathbf{u}}_{\alpha,a}^m(t); \; \hat{\mathbf{u}}_{\alpha,a}^m(t) = \hat{\mathbf{u}}_\alpha(\mathbf{x}_a, t) \text{ if } \mathbf{x}_\alpha \in \Gamma_\alpha^u \right\} \tag{19}$$

in which, N_D and n_{d_α} denote the number of nodes associated with the finite element base in the macroscale discretization of Ω, and the microscale discretization of Ω_α, respectively; N_A is the shape function for the macroscale field and $n_{\alpha,a}$ is the shape function for the microscale response; $\mathbf{x}_A$ and $\mathbf{x}_a$ are the nodal coordinates in the corresponding scale. Overhat denotes

the nodal coefficients of the corresponding response field.

3 Reduced Order Variational Multiscale Enrichment

In the direct variational multiscale enrichment method that was proposed in Refs. [41, 42, 51], the microscale structure is fully discretized into finite elements according to the material heterogeneity, as illustrated in Fig. 1(c). The numerical assessment of the microscale problems is therefore computationally expensive, especially when the microstructure is complicated and the number of enrichment domains is large. In the current manuscript, an eigenstrain-based model reduction technique [43] is employed for efficient evaluation of the microscale problems.

3.1 Numerical evaluation of the microscale problem

We start by decomposing the microscale displacement field as follows:

$$\mathbf{u}_\alpha^m(\mathbf{x}, t) = \sum_{A=1}^{N_D} \mathbf{H}_A^\alpha(\mathbf{x}) \cdot \hat{\mathbf{u}}_A^{M\alpha}(t) + \int_{\Omega_\alpha} \mathbf{h}^\alpha(\mathbf{x}, \hat{\mathbf{x}}) : \boldsymbol{\varepsilon}^{vp}(\hat{\mathbf{x}}, t) \ d\hat{\mathbf{x}} \tag{20}$$

where, $\hat{\mathbf{u}}_A^{M\alpha}$ denotes the macroscale nodal coefficient corresponding to the Ath node of the enrichment domain, Ω_α. $\mathbf{H}_A^\alpha$, a second order tensor, is the linear elastic influence function in Ω_α. $\mathbf{h}^\alpha(\mathbf{x}, \hat{\mathbf{x}})$ $(\mathbf{x}, \hat{\mathbf{x}} \in \Omega_\alpha)$, a third order tensor, is the influence function associated with the inelastic deformation within the enrichment domain. In the absence of inelastic processes, the second term on the right hand side of Eq. (20) vanishes. The microscale displacement field is then expressed using influence functions ($\mathbf{H}_A^\alpha$) acting on the finite element basis (described by the nodal coefficients of the macroscale element over the enrichment domain) leveraging the linearity of the problem as proposed by Refs. [2, 3]. In the presence of inelastic deformation, the second component is obtained by considering the inelastic strain field as spatially variable force acting on the microstructure, and using the Green's function idea to compute the microscale displacement contribution as a function of the spatially variable inelastic strain (eigenstrain) field [7]. Equation (20) is valid under the conditions of small deformation theory and additive split of the strain tensor. In the presence of geometric nonlinearity and plasticity models that employ multiplicative split, this decomposition is not directly valid as the inelastic influence functions become time (or load amplitude) dependent.

The influence functions $\mathbf{H}_A^\alpha$ and $\mathbf{h}^\alpha$ are determined from the microscale weak form shown in Eq. (12). Employing the constitutive equation (i.e., Eq. (13)) and the microscale displacement field discretization defined in Eq. (20), the weak form of the microscale problem becomes

$(\alpha = 1, 2, ...n_{\mathrm{en}})$:

$$\sum_{A=1}^{N_D} \left[\left(\int_{\Omega_\alpha} \nabla \mathbf{w}_\alpha^m : \mathbf{L} : \nabla \mathbf{H}_A^\alpha \, d\Omega \; + \int_{\Omega_\alpha} \nabla \mathbf{w}_\alpha^m : \mathbf{L} \cdot \nabla N_A \, d\Omega \right) \cdot \hat{\mathbf{u}}_A^{M\alpha}(t) \right]$$
$$+ \int_{\Omega_\alpha} \nabla \mathbf{w}_\alpha^m : \mathbf{L} : \left[\int_{\Omega_\alpha} \nabla \mathbf{h}^\alpha(\mathbf{x}, \hat{\mathbf{x}}) : \boldsymbol{\varepsilon}^{vp}(\hat{\mathbf{x}}, t) \, d\hat{\mathbf{x}} - \boldsymbol{\varepsilon}^{vp}(\mathbf{x}, t) \right] d\Omega = 0 \tag{21}$$

Considering the elastic state (i.e., when the enrichment domain undergoes deformation in the absence of the inelastic process), Eq. (21) is reduced to:

$$\sum_{A=1}^{N_D} \left[\left(\int_{\Omega_\alpha} \nabla \mathbf{w}_\alpha^m : \mathbf{L} : \nabla \mathbf{H}_A^\alpha \, d\Omega \; + \int_{\Omega_\alpha} \nabla \mathbf{w}_\alpha^m : \mathbf{L} \cdot \nabla N_A \, d\Omega \right) \cdot \hat{\mathbf{u}}_A^{M\alpha}(t) \right] = 0 \tag{22}$$

We note that the displacement coefficients, $\hat{\mathbf{u}}_A^M$ vary with time only, while $\nabla \mathbf{w}_\alpha^m$ and ∇N_A are functions of the space coordinates with no variation in time. The governing equation for the linear-elastic influence function, $\mathbf{H}_A^\alpha$, then becomes:

$$\int_{\Omega_\alpha} \nabla \mathbf{w}_\alpha^m : \mathbf{L} : \nabla \mathbf{H}_A^\alpha \, d\Omega = \; - \int_{\Omega_\alpha} \nabla \mathbf{w}_\alpha^m : \mathbf{L} \cdot \nabla N_A \, d\Omega; \quad \forall \, A = 1, 2, ..., N_D \tag{23}$$

In the presence of inelastic deformation and in view of Eq. (22), Eq. (21) yields:

$$\int_{\Omega_\alpha} \nabla \mathbf{w}_\alpha^m : \mathbf{L} : \left[\int_{\Omega_\alpha} \nabla \mathbf{h}^\alpha(\mathbf{x}, \hat{\mathbf{x}}) : \boldsymbol{\varepsilon}^{vp}(\hat{\mathbf{x}}, t) \, d\hat{\mathbf{x}} - \boldsymbol{\varepsilon}^{vp}(\mathbf{x}, t) \right] d\Omega = 0 \tag{24}$$

The viscoplastic strain field within the enrichment domain Ω_α is expressed as:

$$\boldsymbol{\varepsilon}^{vp}(\mathbf{x}, t) = \int_{\Omega_\alpha} \delta^d(\mathbf{x} - \hat{\mathbf{x}}) \boldsymbol{\varepsilon}^{vp}(\hat{\mathbf{x}}, t) \, d\hat{\mathbf{x}}; \quad \forall \mathbf{x} \in \Omega_\alpha \tag{25}$$

where δ^d denotes the Dirac delta distribution. Substituting Eq. (25) into Eq. (24) yields the weak form equation for the inelastic influence function $\mathbf{h}^\alpha(\mathbf{x}, \hat{\mathbf{x}})$:

$$\int_{\Omega_\alpha} \nabla \mathbf{w}_\alpha^m : \mathbf{L} : \nabla \mathbf{h}^\alpha(\mathbf{x}, \hat{\mathbf{x}}) \, d\Omega = \int_{\Omega_\alpha} \nabla \mathbf{w}_\alpha^m : \mathbf{L} \, \delta^d(\mathbf{x} - \hat{\mathbf{x}}) \, d\Omega; \quad \forall \hat{\mathbf{x}} \in \Omega_\alpha \tag{26}$$

The influence functions, $\mathbf{H}_A^\alpha$ and $\mathbf{h}^\alpha$, are evaluated numerically. The detailed finite element solution of Eq. (23) is provided in [2, 3]. The numerical evaluation of the inelastic influence function, involving the approximation of the Dirac distribution and the details of a numerical treatment, is provided in Ref. [43]. While possible and straightforward, direct computation of the inelastic influence function is costly and is not needed in the reduced model formulation as further described below. Representing the microscale displacement field with the influence functions $\mathbf{H}_A^\alpha$ ($A = 1, 2, ..., N_D$) and $\mathbf{h}^\alpha$, the microscale weak form, Eq. (21), is automatically

satisfied for arbitrary inelastic strain of macroscale displacement states.

3.2 Reduced order microscale problem

The total number of degrees of freedom in the enrichment domain problem is reduced by replacing the fully resolved microscale discretization with a reduced order microscale partitioning. The reduced order partitioning is performed such that each enrichment domain is decomposed into NP_α subdomains (parts):

$$\Omega_\alpha = \bigcup_{\gamma=1}^{NP_\alpha} \Omega_\gamma^\alpha; \quad \Omega_\gamma^\alpha \cap \Omega_\eta^\alpha \equiv \emptyset \quad \text{when} \quad \gamma \neq \eta \tag{27}$$

where γ and η are the indices of parts in an arbitrary enrichment domain Ω_α. The stress and inelastic strain fields are discretized using the separation of variables as [43]:

$$\boldsymbol{\sigma}(\mathbf{x}, t) = \sum_{\gamma=1}^{NP_\alpha} N_\gamma^\alpha(\mathbf{x})\, \boldsymbol{\sigma}_\gamma^\alpha(t); \quad \boldsymbol{\varepsilon}^{vp}(\mathbf{x}, t) = \sum_{\gamma=1}^{NP_\alpha} N_\gamma^\alpha(\mathbf{x})\, \boldsymbol{\mu}_\gamma^\alpha(t); \quad \mathbf{x} \in \Omega_\alpha \tag{28}$$

where, $\boldsymbol{\sigma}_\gamma^\alpha$ and $\boldsymbol{\mu}_\gamma^\alpha$ are the stress and inelastic strain coefficients, respectively. N_γ^α denotes shape function associated with part Ω_γ^α, such that:

$$N_\gamma^\alpha(\mathbf{x}) = \begin{cases} 1, & \text{if } \mathbf{x} \in \Omega_\gamma^\alpha \\ 0, & \text{elsewhere} \end{cases} \tag{29}$$

The above discretization therefore leads to a piecewise constant approximation of the stress and inelastic strain fields over the enrichment domain. The stress and inelastic strain fields are discontinuous within the enrichment domain, which is consistent with the C^0 continuous finite element approximation of the displacement field. For instance, as the number of parts NP_α reaches the number of elements in the microscale discretization for constant strain elements, the approximations are of the same order. Substituting the reduced order microscale partitioning (Eq. (28)) into Eq. (20), the microscale displacement field becomes:

$$\begin{aligned}
\mathbf{u}_\alpha^m(\mathbf{x}, t) &= \sum_{A=1}^{N_D} \mathbf{H}_A^\alpha(\mathbf{x}) \cdot \hat{\mathbf{u}}_A^{M\alpha}(t) + \sum_{\gamma=1}^{NP_\alpha} \left[\int_{\Omega^\alpha} \mathbf{h}^\alpha(\mathbf{x}, \hat{\mathbf{x}})\, N_\gamma^\alpha(\mathbf{x})\, d\hat{\mathbf{x}} : \boldsymbol{\mu}_\gamma^\alpha(t) \right] \\
&= \sum_{A=1}^{N_D} \mathbf{H}_A^\alpha(\mathbf{x}) \cdot \hat{\mathbf{u}}_A^{M\alpha}(t) + \sum_{\gamma=1}^{NP_\alpha} \left[\int_{\Omega_\gamma^\alpha} \mathbf{h}^\alpha(\mathbf{x}, \hat{\mathbf{x}})\, d\hat{\mathbf{x}} : \boldsymbol{\mu}_\gamma^\alpha(t) \right]
\end{aligned} \tag{30}$$

Similarly, substituting Eq. (28) into Eq. (13), the constitutive equation for enrichment domain Ω_α yields:

$$\sum_{\gamma=1}^{NP_\alpha} N_\gamma^\alpha(\mathbf{x}) \, \boldsymbol{\sigma}_\gamma^\alpha(t) = \sum_{A=1}^{N_D} \mathbf{S}_A^\alpha(\mathbf{x}) \cdot \hat{\mathbf{u}}_A^{M\alpha}(t) + \sum_{\gamma=1}^{NP_\alpha} \mathbf{P}_\gamma^\alpha(\mathbf{x}) : \boldsymbol{\mu}_\gamma^\alpha(t) \tag{31}$$

in which, the coefficient tensors are defined for an arbitrary enrichment domain Ω_α ($\alpha = 1, 2, ..., n_{\mathrm{en}}$) :

$$\mathbf{S}_A^\alpha(\mathbf{x}) = \mathbf{L}(\mathbf{x}) \cdot \nabla N_A(\mathbf{x}) + \mathbf{L}(\mathbf{x}) : \nabla \mathbf{H}_A^\alpha(\mathbf{x}); \quad \forall \, A = 1, 2, ..., N_D \tag{32}$$

and for each part Ω_γ^α ($\gamma = 1, 2, ..., NP_\alpha$):

$$\mathbf{P}_\gamma^\alpha(\mathbf{x}) = \mathbf{L}(\mathbf{x}) : \int_{\Omega_\gamma^\alpha} \nabla \mathbf{h}^\alpha(\mathbf{x}, \hat{\mathbf{x}}) \, d\hat{\mathbf{x}} - \mathbf{L}(\mathbf{x}) \, N_\gamma^\alpha(\mathbf{x}) \tag{33}$$

Integrating both sides of Eq. (31) over part Ω_η^α of enrichment domain Ω_α, the constitutive equation on part η ($\mathbf{x} \in \Omega_\eta^\alpha$) is simplified to:

$$\boldsymbol{\sigma}_\eta^\alpha(t) = \sum_{A=1}^{N_D} \mathbf{S}_{\eta A}^\alpha \cdot \hat{\mathbf{u}}_A^{M\alpha}(t) + \sum_{\gamma=1}^{NP_\alpha} \mathbf{P}_{\eta\gamma}^\alpha : \boldsymbol{\mu}_\gamma^\alpha(t) \tag{34}$$

Since the stress and inelastic strain coefficients are constant on each part, the homogenized coefficient tensors on each part Ω_η^α within the enrichment domain Ω_α is defined as:

$$\mathbf{S}_{\eta A}^\alpha = \frac{1}{|\Omega_\eta^\alpha|} \int_{\Omega_\eta^\alpha} \mathbf{S}_A^\alpha(\mathbf{x}) \, d\Omega; \quad \mathbf{x} \in \Omega_\eta^\alpha \tag{35}$$

$$\mathbf{P}_{\eta\gamma}^\alpha = \frac{1}{|\Omega_\eta^\alpha|} \int_{\Omega_\eta^\alpha} \mathbf{P}_\gamma^\alpha(\mathbf{x}) \, d\Omega; \quad \mathbf{x} \in \Omega_\eta^\alpha \tag{36}$$

The time-independent coefficient tensors, $\mathbf{S}_{\eta A}^\alpha$ and $\mathbf{P}_{\eta\gamma}^\alpha$, are obtained using the influence functions, $\mathbf{H}_A^\alpha$ and $\mathbf{h}^\alpha$. Since the influence functions satisfy the microscale equilibrium, as discussed in Section 3.1, the stresses computed using the coefficient tensors, $\mathbf{S}_{\eta A}^\alpha$ and $\mathbf{P}_{\eta\gamma}^\alpha$, automatically satisfy microscale equilibrium for arbitrary macroscale displacement and inelastic strain coefficients. The corresponding rate-form constitutive equation is:

$$\dot{\boldsymbol{\sigma}}_\eta^\alpha(t) = \sum_{A=1}^{N_D} \mathbf{S}_{\eta A}^\alpha \cdot \dot{\hat{\mathbf{u}}}_A^{M\alpha}(t) + \sum_{\gamma=1}^{NP_\alpha} \mathbf{P}_{\eta\gamma}^\alpha : \dot{\boldsymbol{\mu}}_\gamma^\alpha(t) \tag{37}$$

Remark 2. In the direct VME method where the microstructural features are fully resolved, the number of degrees of freedom (DOFs) depends on the resolution of the finite element discretization. In contrast, the number of DOFs in the reduced order VME method depends on the number of parts (i.e., NP_α) within the microstructural partitioning. In order to achieve computational efficiency, the order of the discretization in Eq. (28) is chosen to be much smaller than the DOFs associated with the direct finite element discretization of the enrichment domain. The manner in which the partitioning is made, as well as the order of the model, impacts the accuracy characteristics of the reduced order model. The effects of different partitioning strategies have been discussed in the context of computational homogenization in Ref. [43]. It is also possible to choose shape functions that are not piecewise constant [36, 37, 46].

Remark 3. The integration of the gradient of the inelastic influence function, $\tilde{\mathbf{P}}_\gamma^\alpha(\mathbf{x}) \equiv \int_{\Omega_\gamma^\alpha} \nabla \mathbf{h}^\alpha(\mathbf{x}, \hat{\mathbf{x}}) \, d\hat{\mathbf{x}}$, is needed in the reduced order microscale problem, instead of the inelastic influence function itself, $\mathbf{h}^\alpha(\mathbf{x}, \hat{\mathbf{x}})$. Direct assessment of $\tilde{\mathbf{P}}_\gamma^\alpha$ is performed and the evaluation of $\mathbf{h}^\alpha(\mathbf{x}, \hat{\mathbf{x}})$ in Eq. (26) is skipped which eliminates unnecessary a-priori computations. Substituting Eq. (28) into Eq. (24) yields the weak form equation of $\tilde{\mathbf{P}}_\gamma^\alpha(\mathbf{x})$ for each part Ω_γ^α $(\gamma = 1, 2, ..., NP_\alpha)$:

$$\int_{\Omega_\alpha} \nabla \mathbf{w}_\alpha^m : \mathbf{L} : \tilde{\mathbf{P}}_\gamma^\alpha(\mathbf{x}) \, d\Omega = \int_{\Omega_\alpha} \nabla \mathbf{w}_\alpha^m : \mathbf{L} : N_\gamma^\alpha(\mathbf{x}) \, d\Omega \qquad (38)$$

4 Computational Implementation

This section provides the detailed decomposition of the numerical implementation of the reduced order variational multiscale enrichment method, including the implementation of the reduced order microscale problem, upscaled macroscale problem and a solution algorithm.

A Newton-Raphson iterative scheme is employed to numerically assess the elasto-viscoplastic problem described in this documentation. Consider a discrete set of instances with the observation period: $\{0, {}_1t, {}_2t, ..., {}_nt, {}_{n+1}t, ..., t_o\}$. The viscoplastic slip evolution is discretized based on a one-parameter family (referred to as θ-rule):

$$\dot{\varepsilon}^{vp}(\mathbf{x}, t) = (1 - \theta)\dot{\varepsilon}^{vp}(\mathbf{x}, {}_nt) + \theta\dot{\varepsilon}^{vp}(\mathbf{x}, {}_{n+1}t); \quad t \in [{}_nt, \ {}_{n+1}t] \qquad (39)$$

where $\theta \in [0, 1]$ is an algorithmic parameter. The left subscript n and $n+1$ indicate the value of a field variable at ${}_nt$ and ${}_{n+1}t$, respectively (e.g. ${}_n\varepsilon^{vp} = \varepsilon^{vp}({}_nt)$). Note $N_\eta^\alpha(\mathbf{x}) = 0 \ \forall \eta \neq \gamma$

13

when $\mathbf{x} \in \Omega_\gamma^\alpha$. Employing the rate form of the inelastic strain coefficients (i.e., Eq. (28)), for each part Ω_γ^α in the enrichment domain Ω_α, Eq. (39) is equivalent to:

$$\dot{\boldsymbol{\mu}}_\gamma^\alpha(t) = (1-\theta)\ \dot{\boldsymbol{\mu}}_\gamma^\alpha(\mathbf{x},\,{}_n t) + \theta\ \dot{\boldsymbol{\mu}}_\gamma^\alpha(\mathbf{x},\,{}_{n+1}t); \quad t \in \left[{}_n t,\ {}_{n+1}t\right] \tag{40}$$

Correspondingly, the evolution equation for the inelastic coefficient, $\dot{\boldsymbol{\mu}}_\gamma^\alpha$, is obtained from Eq. (14) as:

$$\dot{\boldsymbol{\mu}}_\gamma^\alpha(\boldsymbol{\sigma}_\gamma^\alpha, \boldsymbol{\mu}_\gamma^\alpha) = \gamma \left\langle \frac{\sqrt{3}\bar{\sigma}(\boldsymbol{\sigma}_\gamma^\alpha) - \sigma_y(\boldsymbol{\mu}_\gamma^\alpha)}{\sigma_y(\boldsymbol{\mu}_\gamma^\alpha)} \right\rangle^q \frac{\partial f(\boldsymbol{\sigma}_\gamma^\alpha, \boldsymbol{\mu}_\gamma^\alpha)}{\partial \boldsymbol{\sigma}_\gamma^\alpha} \tag{41}$$

4.1 Numerical evaluation of the reduced order microscale problem

The nonlinear microscale problem defined by Eqs. (37), (40) and (41) is evaluated using the Newton-Raphson iterative scheme. Substituting Eq. (40) into Eq. (37), the time discretization of the residual of the constitutive equation for an arbitrary part Ω_η^α becomes:

$$\begin{aligned}
\mathbf{R}_\eta^\alpha \equiv\ &{}_{n+1}\boldsymbol{\sigma}_\eta^\alpha - {}_n\boldsymbol{\sigma}_\eta^\alpha - \sum_{A=1}^{N_D} \mathbf{S}_{\eta A}^\alpha \cdot \left({}_{n+1}\hat{\mathbf{u}}_A^{M\alpha} - {}_n\hat{\mathbf{u}}_A^{M\alpha}\right) \\
&- (1-\theta)\ \Delta t \sum_{\gamma=1}^{NP_\alpha} \mathbf{P}_{\eta\gamma}^\alpha : {}_n\dot{\boldsymbol{\mu}}_\gamma^\alpha - \theta\ \Delta t \sum_{\gamma=1}^{NP_\alpha} \mathbf{P}_{\eta\gamma}^\alpha : {}_{n+1}\dot{\boldsymbol{\mu}}_\gamma^\alpha = 0
\end{aligned} \tag{42}$$

In what follows, the left subscript $n+1$ of the fields at current configuration is omitted for clarity of presentation. Considering a first order Taylor series approximation of Eq. (42) and forming a Newton iteration yield the following residual for the stress-strain equation:

$$\begin{aligned}
\mathbf{R}_\eta^{\alpha,k+1} \approx\ \mathbf{R}_\eta^{\alpha,k} + &\sum_{\gamma=1}^{NP_\alpha} \left[\left(\delta_{\eta\gamma}^K\ \mathbf{I} - \theta\ \Delta t\ \mathbf{P}_{\eta\gamma}^\alpha : \mathbf{C}_\gamma^{\alpha,k} \right) : \delta\boldsymbol{\sigma}_\gamma^\alpha \right] \\
&- \theta\ \Delta t \sum_{\gamma=1}^{NP_\alpha} \left[\mathbf{P}_{\eta\gamma}^\alpha : \mathbf{G}_\gamma^{\alpha,k} : \delta\boldsymbol{\mu}_\gamma^\alpha \right] - \sum_{A=1}^{N_D} \left[\mathbf{S}_{\eta A}^\alpha \cdot \delta\hat{\mathbf{u}}_A^{M\alpha} \right] = 0
\end{aligned} \tag{43}$$

in which, superscript k denotes Newton iteration counter; $\delta(\cdot)$ indicates the increment of response field $(\cdot)$ during the current iteration (e.g., $\delta\hat{\mathbf{u}}_A^M = \hat{\mathbf{u}}_A^{M,k+1} - \hat{\mathbf{u}}_A^{M,k}$). $\delta_{\eta\gamma}^K$ is the Kronecker delta; $\mathbf{I}$ the fourth order identity tensor; and

$$\mathbf{C}_\gamma^{\alpha,k} = \left(\frac{\partial\dot{\boldsymbol{\mu}}_\gamma^\alpha}{\partial\boldsymbol{\sigma}_\gamma^\alpha}\right)^k; \quad \mathbf{G}_\gamma^{\alpha,k} = \left(\frac{\partial\dot{\boldsymbol{\mu}}_\gamma^\alpha}{\partial\boldsymbol{\mu}_\gamma^\alpha}\right)^k \tag{44}$$

14

The explicit expressions for $\mathbf{C}_\gamma^{\alpha,k}$ and $\mathbf{G}_\gamma^{\alpha,k}$ are provided in the Appendix. Note $\mathbf{C}_\gamma^{\alpha,k}$ and $\mathbf{G}_\gamma^{\alpha,k}$ are constant over each part Ω_γ^α.

The residual of the kinematic equation (i.e., Eq. (40)) is defined as:

$$\boldsymbol{\lambda}_\gamma^\alpha \equiv \boldsymbol{\mu}_\gamma^\alpha - {}_n\boldsymbol{\mu}_\gamma^\alpha - \Delta t \, (1-\theta) \, {}_n\dot{\boldsymbol{\mu}}_\gamma^\alpha - \Delta t \, \theta \, \dot{\boldsymbol{\mu}}_\gamma^\alpha = 0 \tag{45}$$

Expanding Eq. (45) using the first order Taylor series approximation, the inelastic coefficient increment at the current Newton iteration is expressed in terms of the stress coefficient as:

$$\delta\boldsymbol{\mu}_\gamma^\alpha = \left(\mathbf{I} - \theta \, \Delta t \, \mathbf{G}_\gamma^{\alpha,k}\right)^{-1} : \left(\theta \, \Delta t \, \mathbf{C}_\gamma^{\alpha,k}\right) : \delta\boldsymbol{\sigma}_\gamma^\alpha - \left(\mathbf{I} - \theta \, \Delta t \, \mathbf{G}_\gamma^{\alpha,k}\right)^{-1} : \boldsymbol{\lambda}_\gamma^{\alpha,k} \tag{46}$$

Substituting Eq. (46) into Eq. (43), the inelastic coefficients are condensed out to yield:

$$\sum_{\gamma=1}^{NP_\alpha} \left(\mathbf{Q}_{\eta\gamma}^{\alpha,k} : \delta\boldsymbol{\sigma}_\gamma^\alpha\right) = \sum_{A=1}^{N_D} \left(\mathbf{S}_{\eta A}^\alpha : \delta\hat{\mathbf{u}}_A^{M\alpha}\right) - \mathbf{V}_\eta^{\alpha,k} \tag{47}$$

where,

$$\mathbf{Q}_{\eta\gamma}^{\alpha,k} = \delta_{\eta\gamma}^K \, \mathbf{I} - \theta \, \Delta t \, \mathbf{P}_{\eta\gamma}^\alpha : \mathbf{C}_\gamma^{\alpha,k} - (\theta \, \Delta t)^2 \, \mathbf{P}_{\eta\gamma}^\alpha : \mathbf{G}_\gamma^{\alpha,k} : \left(\mathbf{I} - \theta \, \Delta t \, \mathbf{G}_\gamma^{\alpha,k}\right)^{-1} : \mathbf{C}_\gamma^{\alpha,k} \tag{48}$$

$$\mathbf{V}_\eta^{\alpha,k} = \mathbf{R}_\eta^{\alpha,k} + \theta \, \Delta t \, \sum_{\gamma=1}^{NP_\alpha} \left[\mathbf{P}_{\eta\gamma}^\alpha : \mathbf{G}_\gamma^{\alpha,k} : \left(\mathbf{I} - \theta \, \Delta t \, \mathbf{G}_\gamma^{\alpha,k}\right)^{-1} : \boldsymbol{\lambda}_\gamma^{\alpha,k}\right] \tag{49}$$

Considering $\eta = 1, 2, ..., NP_\alpha$ in Eq. (47) separately, the stress increment vector at the enrichment domain Ω_α which contains stress increment within each part of the enrichment domain is obtained as:

$$\delta\boldsymbol{\sigma}^\alpha = \left(\mathbf{Q}^{\alpha,k}\right)^{-1} \mathbf{S}^\alpha \, \delta\hat{\mathbf{u}}^{M\alpha} - \left(\mathbf{Q}^{\alpha,k}\right)^{-1} \mathbf{V}^{\alpha,k} \tag{50}$$

where $\mathbf{Q}^{\alpha,k}$ and $\mathbf{S}^\alpha$ are coefficient tensors defined as:

$$\mathbf{Q}^{\alpha,k} = \left[\mathbf{Q}_{\eta\gamma}^{\alpha,k}\right]_{\eta,\gamma\in[1,NP_\alpha]}; \qquad \mathbf{S}^\alpha = \left[\mathbf{S}_{\eta A}^\alpha\right]_{\eta\in[1,NP_\alpha],A\in[1,N_D]} \tag{51}$$

and

$$\delta\boldsymbol{\sigma}^\alpha = \left\{\left(\delta\boldsymbol{\sigma}_1^{\alpha,k+1}\right)^T, \left(\delta\boldsymbol{\sigma}_2^{\alpha,k+1}\right)^T, ..., \left(\delta\boldsymbol{\sigma}_{NP_\alpha}^{\alpha,k+1}\right)^T\right\}^T \tag{52a}$$

$$\delta\hat{\mathbf{u}}^{M\alpha} = \left\{\left(\delta\hat{\mathbf{u}}_1^{M\alpha,k+1}\right)^T, \left(\delta\hat{\mathbf{u}}_2^{M\alpha,k+1}\right)^T, ..., \left(\delta\hat{\mathbf{u}}_{N_D}^{M\alpha,k+1}\right)^T\right\}^T \tag{52b}$$

$$\mathbf{V}^{\alpha,k} = \left\{\left(\mathbf{V}_1^{\alpha,k}\right)^T, \left(\mathbf{V}_2^{\alpha,k}\right)^T, ..., \left(\mathbf{V}_{NP_\alpha}^{\alpha,k}\right)^T\right\}^T \tag{52c}$$

15

4.2 Numerical evaluation of the macroscale problem

For the substrate region Ω_s, the finite element discretization of the macroscale equations is standard [51] and only briefly described when necessary. This subsection particularly focuses on the treatment of the macroscale problem in the enrichment region. The macroscale weak form is linearized to construct a Newton-Raphson iterative scheme, employing the linearized reduced order microscale problem stated in the previous section.

Considering the decomposition of the problem domain introduced in Eqs. (5) and (6), the residual of the macroscale weak form is defined as:

$$\boldsymbol{\Psi}^M \equiv \sum_{\alpha=1}^{n_{\mathrm{en}}} \tilde{\boldsymbol{\Psi}}_\alpha^M + \tilde{\boldsymbol{\Psi}}_s^M - \sum_{\alpha=1}^{n_{\mathrm{en}}} \tilde{\boldsymbol{\Psi}}_\alpha^{MT} - \tilde{\boldsymbol{\Psi}}_s^{MT} = 0 \tag{53}$$

where,

$$\tilde{\boldsymbol{\Psi}}_\alpha^M = \int_{\Omega_\alpha} \nabla \mathbf{w}^M : \boldsymbol{\sigma}(\hat{\mathbf{u}}^M, \hat{\mathbf{u}}_\alpha^m) \ d\Omega; \quad \tilde{\boldsymbol{\Psi}}_s^M = \int_{\Omega_s} \nabla \mathbf{w}^M : \boldsymbol{\sigma}(\hat{\mathbf{u}}^M) \ d\Omega \tag{54}$$

$$\tilde{\boldsymbol{\Psi}}_\alpha^{MT} = \int_{\Gamma_\alpha^t} \mathbf{w}^M \cdot \tilde{\mathbf{t}} \ d\Gamma; \quad \tilde{\boldsymbol{\Psi}}_s^{MT} = \int_{\Gamma_s^t} \mathbf{w}^M \cdot \tilde{\mathbf{t}} \ d\Gamma \tag{55}$$

Γ_α^t is the part of the enrichment domain boundary that intersects with the Neumann boundary of the problem domain ($\Gamma_\alpha^t \equiv \Gamma_\alpha \cap \Gamma^t$); and, Γ_s^t is the part of the substrate region boundary that intersects with the Neumann boundary of the problem domain ($\Gamma_s^t \equiv \Gamma_s \cap \Gamma^t$). Within the substrate region, Ω_s, the microstructural displacement remains unresolved. The stress field therefore is a function of the macroscale displacement field only.

Substituting Eq. (28) into Eq. (53), the residual of the macroscale weak form within the enrichment domain, Ω_α, is expressed as:

$$\tilde{\boldsymbol{\Psi}}_\alpha^M = \sum_{\gamma=1}^{NP_\alpha} \int_{\Omega_\gamma^\alpha} \nabla \mathbf{w}^M \ d\Omega : \boldsymbol{\sigma}_\gamma^\alpha(t) \tag{56}$$

Employing the expression of $\tilde{\boldsymbol{\Psi}}_\alpha^M$ in Eq. (56) and considering the first order Taylor series approximation, the residual of the macroscale weak form (i.e., Eq. (53)) becomes:

$$\boldsymbol{\Psi}^{M,k+1} \approx \sum_{\alpha=1}^{n_{\mathrm{en}}} \left(\tilde{\boldsymbol{\Psi}}_\alpha^{M,k+1} \right) + \tilde{\boldsymbol{\Psi}}_s^{M,k+1} = 0 \tag{57}$$

where,

$$\tilde{\boldsymbol{\Psi}}_\alpha^{M,k+1} \equiv \tilde{\boldsymbol{\Psi}}_\alpha^{M,k} - \tilde{\boldsymbol{\Psi}}_\alpha^{MT} + \delta \tilde{\boldsymbol{\Psi}}_\alpha^M; \quad \tilde{\boldsymbol{\Psi}}_s^{M,k+1} \equiv \tilde{\boldsymbol{\Psi}}_s^{M,k} - \tilde{\boldsymbol{\Psi}}_s^{MT} + \delta \tilde{\boldsymbol{\Psi}}_s^M \tag{58}$$

and

$$\delta \tilde{\boldsymbol{\Psi}}_\alpha^M = \sum_{\gamma=1}^{NP_\alpha} \left(\int_{\Omega_\gamma^\alpha} \nabla \mathbf{w}^M \ d\Omega \right) : \delta \boldsymbol{\sigma}_\gamma^\alpha; \quad \delta \tilde{\boldsymbol{\Psi}}_s^M = \int_{\Omega_s} \nabla \mathbf{w}^M : \delta \boldsymbol{\sigma}(\delta \hat{\mathbf{u}}^M) \ d\Omega \tag{59}$$

$\tilde{\mathbf{\Psi}}_\alpha^{MT}$ and $\tilde{\mathbf{\Psi}}_s^{MT}$ denote the prescribed boundary traction terms which do not vary with iterations at a given time step.

Using the standard finite element discretization detailed in Eq. (18) for the macroscale test function $\mathbf{w}^M$, $\delta\tilde{\mathbf{\Psi}}_\alpha^M$ (Eq. (59)) yields:

$$\delta\tilde{\mathbf{\Psi}}_\alpha^M = \sum_{\gamma=1}^{NP_\alpha} \left[\sum_{A=1}^{N_D} \left(\int_{\Omega_\gamma^\alpha} \nabla N_A \, d\Omega \, \hat{\mathbf{w}}_A^M \right) : \delta\boldsymbol{\sigma}_\gamma^\alpha \right] \tag{60}$$

Considering the stress increment (i.e., $\delta\boldsymbol{\sigma}^\alpha$) defined in Eq. (52a), the matrix form of Eq. (60) is presented as:

$$\delta\tilde{\mathbf{\Psi}}_\alpha^M = (\mathbf{B}^\alpha)^{\mathrm{T}} \, \delta\boldsymbol{\sigma}^\alpha \tag{61}$$

where,

$$\mathbf{B}^\alpha = \left[\mathbf{B}_{\gamma A}^\alpha\right]_{\gamma\in[1,NP_\alpha],A\in[1,N_D]} ; \qquad \mathbf{B}_{\gamma A}^\alpha = \int_{\Omega_\gamma^\alpha} \nabla N_A \, d\Omega \, \hat{\mathbf{w}}_A^M \tag{62}$$

Substituting the stress coefficient increment (i.e. Eq. (50)) and Eq. (61) into Eq. (58), the weak form residual of the enrichment domain at the current iteration is presented in the vector-matrix form as:

$$\tilde{\mathbf{\Psi}}_\alpha^{M,k+1} = \mathbf{K}^\alpha \, \delta\hat{\mathbf{u}}^{M\alpha} - \delta\mathbf{f}^\alpha \tag{63}$$

where,

$$\mathbf{K}^\alpha = (\mathbf{B}^\alpha)^{\mathrm{T}} \left(\mathbf{Q}^{\alpha,k}\right)^{-1} \mathbf{S}^\alpha \tag{64}$$

$$\delta\mathbf{f}^\alpha = (\mathbf{B}^\alpha)^{\mathrm{T}} \left(\mathbf{Q}^{\alpha,k}\right)^{-1} \mathbf{V}^{\alpha,k} - \tilde{\mathbf{\Psi}}_\alpha^{M,k} + \tilde{\mathbf{\Psi}}_\alpha^{MT} \tag{65}$$

The detailed formulation and the standard finite element discretization of $\tilde{\mathbf{\Psi}}_s^{M,k+1}$ is presented in [51] and not repeated in the current documentation for brevity.

Assembling the macroscale element stiffness matrices and force increment vectors, the discrete macroscale weak form (i.e., Eq. (57)) at the $(k+1)^{\mathrm{th}}$ iteration of the current time step, $_{n+1}t$, is expressed as:

$$\mathbf{K} \, \delta\hat{\mathbf{u}}^M = \delta\mathbf{f} \tag{66}$$

where,

$$\mathbf{K} = \mathop{\mathbf{A}}_{e} \mathbf{K}^e \tag{67}$$

$$\delta\hat{\mathbf{u}}^M = \left\{ \left(\delta\hat{\mathbf{u}}_1^{M,k+1}\right)^T, \left(\delta\hat{\mathbf{u}}_2^{M,k+1}\right)^T, ..., \left(\delta\hat{\mathbf{u}}_{N_D}^{M,k+1}\right)^T \right\}^T \tag{68}$$

$$\delta\mathbf{f} = \mathop{\mathbf{A}}_{e} \delta\mathbf{f}^e \tag{69}$$

$\mathbf{A}$ denotes the standard finite element assembly operator and e is the dummy index for all
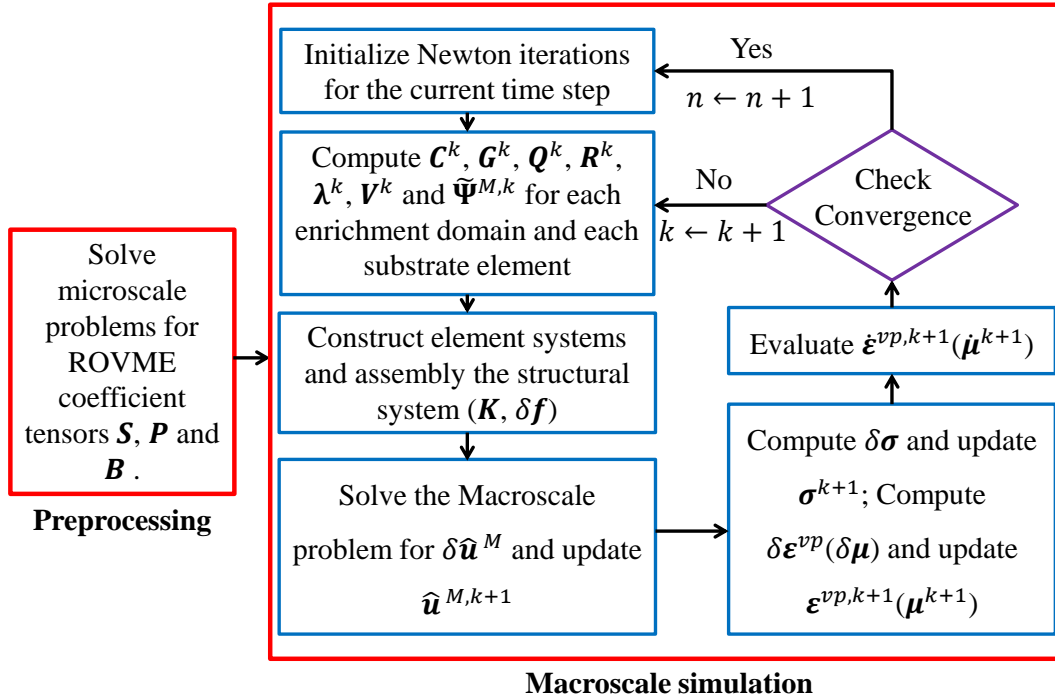
17

Figure 2: Reduced order model implementation strategy.

the macroscale finite elements in the problem domain. The linearized system of equations is evaluated incrementally using the implementation algorithm described in the next subsection.

4.3 Implementation algorithm

The reduced order variational multiscale enrichment (ROVME) method is implemented using the commercial software package, Diffpack [29]. Diffpack provides a library of C++ classes to facilitate the development of solution algorithms for complex PDEs. The overall solution strategy is summarized in Fig. 2, in which the enrichment domain superscript (α) and part subscript (γ) are omitted for clarity. In the preprocessing phase prior to the macroscale simulation, $\mathbf{S}_{\eta A}^{\alpha}$, $\mathbf{P}_{\eta\gamma}^{\alpha}$, $\mathbf{S}^{\alpha}$ and $\mathbf{B}^{\alpha}$ for each enrichment domain Ω_{α} are computed using Eqs. (35), (36), (51) (62) and stored ($A = 1, 2, ..., N_D; \gamma = 1, 2, ..., NP_{\alpha}$ and $\eta = 1, 2, ..., NP_{\alpha}$). They remain constant throughout the macroscale simulation. At an arbitrary time $_n t$, the system is in equilibrium with the constitutive relations satisfied for the problem domain. The algorithm seeks to find the equilibrium state at $_{n+1}t$ as follows:

$Given$: $_n\hat{\mathbf{u}}^M, {}_n\boldsymbol{\sigma}, {}_n\boldsymbol{\varepsilon}^{vp}$ and $_n\dot{\boldsymbol{\varepsilon}}^{vp}$ ($_n\boldsymbol{\mu}_{\gamma}^{\alpha}$ and $_n\dot{\boldsymbol{\mu}}_{\gamma}^{\alpha}$ for enrichment domains) at time $_n t$.

$Find$: $\hat{\mathbf{u}}^M, \boldsymbol{\sigma}, \boldsymbol{\varepsilon}^{vp}$ and $\dot{\boldsymbol{\varepsilon}}^{vp}$ ($\boldsymbol{\mu}_{\gamma}^{\alpha}$ and $\dot{\boldsymbol{\mu}}_{\gamma}^{\alpha}$ for enrichment domains) at time $_{n+1}t$.

1. Initialize Newton iterations by setting: k=0, $\hat{\mathbf{u}}^{M,0} = {}_n\hat{\mathbf{u}}^M$, $\boldsymbol{\sigma}^0 = {}_n\boldsymbol{\sigma}$, $\boldsymbol{\varepsilon}^{vp,0} = {}_n\boldsymbol{\varepsilon}^{vp}$, and $\dot{\boldsymbol{\varepsilon}}^{vp,0} = {}_n\dot{\boldsymbol{\varepsilon}}^{vp}$ ($\boldsymbol{\mu}_{\gamma}^{\alpha,0} = {}_n\boldsymbol{\mu}_{\gamma}^{\alpha}$, and $\dot{\boldsymbol{\mu}}_{\gamma}^{\alpha,0} = {}_n\dot{\boldsymbol{\mu}}_{\gamma}^{\alpha}$ for enrichment domains).

18

2. While not converged, loop over all the macroscale elements within the problem domain Ω for the current iteration $(k+1)$:

   (1) If the macroscale element is enriched:

   a) Compute $\mathbf{C}_\gamma^{\alpha,k}$, $\mathbf{G}_\gamma^{\alpha,k}$, $\mathbf{Q}_{\eta\gamma}^{\alpha,k}$, $\mathbf{R}_\eta^{\alpha,k}$, $\boldsymbol{\lambda}_\eta^{\alpha,k}$, $\mathbf{V}_\eta^{\alpha,k}$, $\tilde{\boldsymbol{\Psi}}_\alpha^{M,k}$ from Eqs. (44), (48), (42), (45), (49) and (56).

   b) Construct $\mathbf{Q}^{\alpha,k}$ and $\mathbf{V}^{\alpha,k}$ from Eqs. (51) and (52c); and $\mathbf{K}^\alpha$ and $\delta\mathbf{f}^\alpha$ from Eqs. (64) and (65).

   (2) If the macroscale element is not enriched :

   a) Compute $\mathbf{K}^e$ and $\delta\mathbf{f}^e$ using the standard finite element procedure [51].

   (3) Employing Eqs. (67) and (69), construct the stiffness matrix $\mathbf{K}$ and incremental force vector $\delta\mathbf{f}$ for the macroscale problem.

   (4) Solve the macroscale problem (Eq. (66)) for $\delta\hat{\mathbf{u}}^M$ and update the macroscale displacement field with $\hat{\mathbf{u}}^{M,k+1} = \hat{\mathbf{u}}^{M,k} + \delta\hat{\mathbf{u}}^M$.

   (5) If the macroscale element is enriched:

   a) Compute the stress increment $\delta\boldsymbol{\sigma}^\alpha$ using Eq. (50) and update the stress field $\boldsymbol{\sigma}^{\alpha,k+1} = \boldsymbol{\sigma}^{\alpha,k} + \delta\boldsymbol{\sigma}^\alpha$.

   b) Compute the inelastic strain coefficient increment $\delta\boldsymbol{\mu}_\gamma^\alpha$ using Eq. (46). Update the inelastic strain coefficient $\boldsymbol{\mu}_\gamma^{\alpha,k+1} = \boldsymbol{\mu}_\gamma^{\alpha,k} + \delta\boldsymbol{\mu}_\gamma^\alpha$.

   c) Evaluate the inelastic strain rate coefficient $\dot{\boldsymbol{\mu}}_\gamma^\alpha$ through Eq. (41).

   (6) If the macroscale element is not enriched:

   a) Determine the stress increment $\delta\boldsymbol{\sigma}$. Update the stress field $\boldsymbol{\sigma}^{k+1} = \boldsymbol{\sigma}^k + \delta\boldsymbol{\sigma}$ [51].

   b) Determine the inelastic strain increment $\delta\boldsymbol{\varepsilon}^{vp,k+1}$. Update the inelastic strain field $\boldsymbol{\varepsilon}^{vp,k+1} = \boldsymbol{\varepsilon}^{vp,k} + \delta\boldsymbol{\varepsilon}^{vp,k+1}$ [51].

   c) Evaluate the inelastic strain rate $\dot{\boldsymbol{\varepsilon}}^{vp,k+1}$ from Eq. (14).

   (7) Check for convergence:

   $$\mathrm{e}^M = \frac{\|\hat{\mathbf{u}}^{M,k+1} - \hat{\mathbf{u}}^{M,k}\|_2}{\|\hat{\mathbf{u}}^{M,k+1} - {}_n\hat{\mathbf{u}}^M\|_2} \leq \text{Convergence tolerance} \qquad (70)$$

   (8) If convergence is not satisfied, set iteration counter $k \leftarrow k+1$ and proceed with the next iteration.

3. Repeat step 2 with $n \leftarrow n+1$ until the end of the observation period.

Remark 4. The convergence of the algorithm is checked for the macroscale displacement field only. As described in Sections 3.1 and 3.2, all enrichment domain problems satisfy equilibrium automatically. No separate convergence check is therefore necessary for the enrichment domains which accelerates the convergence rate for the overall inelastic problem compared with the direct VME method [51].

Remark 5. For explicit computational scheme, $\theta = 0$, $\left(\mathbf{Q}^{\alpha,k}\right)^{-1}$ and $\mathbf{K}^{\alpha}$ remain constant during the numerical procedure. Repeated evaluation of $\left(\mathbf{Q}^{\alpha,k}\right)^{-1}$ and $\mathbf{K}^{\alpha}$ at each iteration is therefore not performed. While this reduces the computational cost of the simulations, the standard stability arguments and time step size restrictions apply.

5 Numerical Verification

The reduced order VME (ROVME) method for elasto-viscoplastic problems is thoroughly verified using numerical simulations. The performance and accuracy characteristics of the ROVME approach are assessed by comparing the results with those of the direct VME simulations. The accuracy characteristics of the direct VME method compared with full resolution finite element analyses was previously demonstrated in Refs. [41, 42, 51].

In all simulations considered in this section, the domains are taken to consist of three separate materials. The heterogeneous material microstructure consists of two phases. A third material that approximates the properties of the composite domain is employed to idealize the behavior at the substrate. The material properties of the two elasto-viscoplastic phases and the corresponding substrate are summarized in Table 1 and the stress-strain curves of these materials under uniaxial tension are plotted in Fig. 3. The phase I material of the microstructure behaves similarly to high yield stress commercially pure titanium [1]. The phase II material is based on low yield stress commercially pure titanium [1]. The properties of the substrate material are obtained using the mixed theory. While the numerical examples provided below investigate two-phase microstructures, the proposed formulation is applicable to arbitrary number of phases and microstructural configurations. A number of multiscale approaches, such as computational homogenization [14, 28, 52] and sequential multiscale modeling [19], also remain valid to compute the homogenized macroscale behavior in the presence of multiple phases within the microstructure. These approaches could be used to compute the substrate domain response.

Table 1: Materials parameters used in the numerical verification studies.

Material type	E [GPa]	ν	A [MPa]	B [MPa]	ε_f	n	q	γ [MPa/hr]
Phase I	107	0.32	480	700	0.15	0.90	1.0	1.0
Phase II	87	0.32	360	100	0.17	0.96	1.0	1.0
Substrate	97	0.32	420	400	0.16	0.93	1.0	1.0
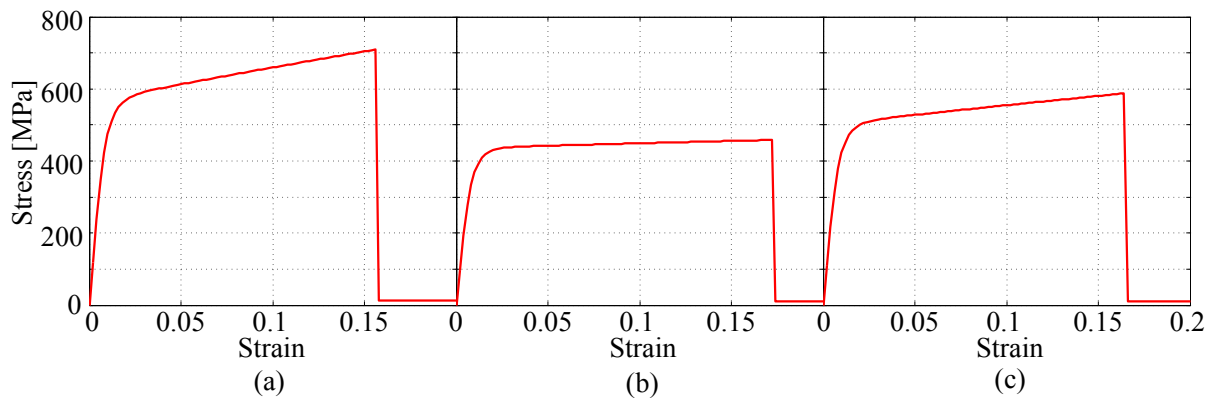
Figure 3: Stress-strain behavior of the constituent materials under uniaxial tension: (a) phase I; (b) phase II; and (c) substrate material.
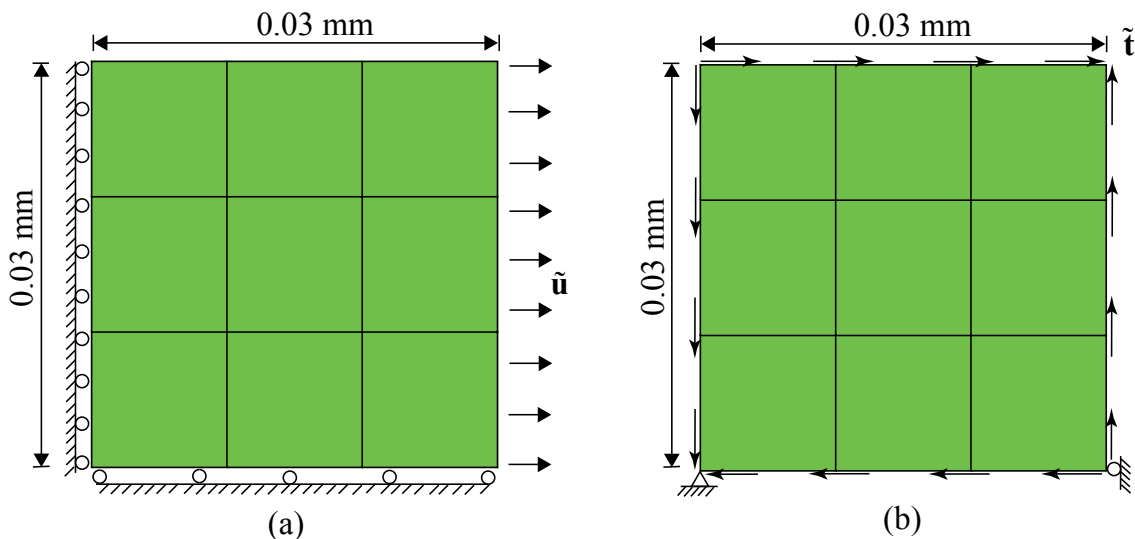
Figure 4: Numerical models of the square specimen: (a) macroscale discretization and sketch for uniform tensile load; and (b) macroscale discretization and sketch for pure shear load.
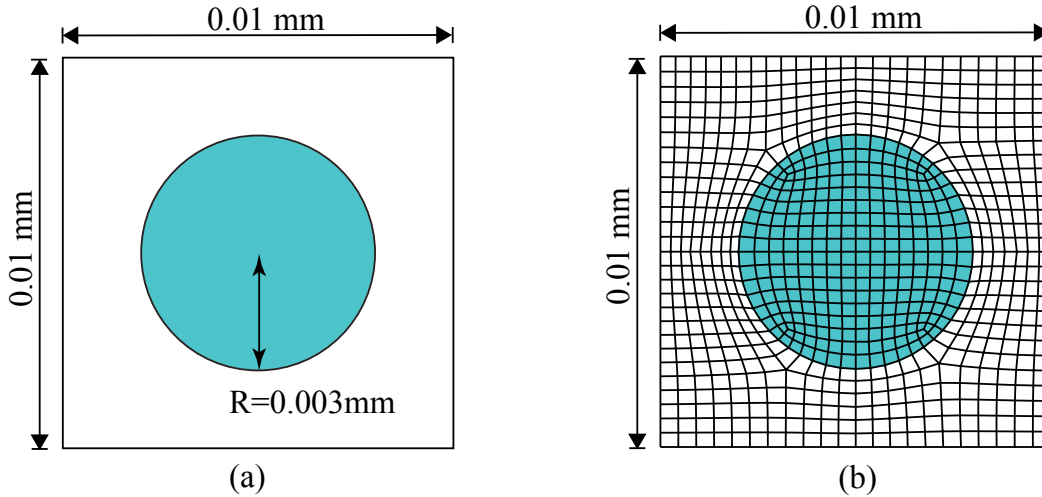
Figure 5: Microscale discretization of an enrichment domain with a circular inclusion: (a) reduced order VME method with 2 parts; and (b) direct VME method.

5.1 Square specimen with circular inclusions

A 2-D plane strain, 0.03 mm × 0.03 mm, square composite specimens are considered to assess the performance of the proposed reduced order VME method. The macroscale discretization and the loading conditions of the specimens are presented in Fig. 4. The macroscale discretization contains 16 nodes and 9 quadrilateral, bilinear finite elements. Each of the 9 macroscale elements is considered as an enrichment domain and associated with a microstructure containing a circular inclusion at the center, as shown in Fig. 5. The ratio between the size of the enrichment domain and the specimen domain is therefore 1/3. Phase I and phase II materials are identified as dark and light elements, respectively. The reduced order VME microscale partitioning consists of 2 parts and 6 degrees of freedom (DOFs). The direct VME microscale grid contains 837 nodes, 786 quadrilateral finite elements and 1674 DOFs. The behavior of the square composite domain is investigated under displacement controlled uniform tension and shear loading conditions. The loading is applied at the strain rate of approximately 3×10^{-4}/sec, until the specimen is about to fail (assessed based on ductility stated in Fig. 3). The time step size is determined such that further refinement does not change the results significantly. The time step size employed in the simulations is set to 0.36 second and the convergence tolerance is set to 1×10^{-3}.

Figure 6 compares the reaction force of the structure vs. the applied displacement as computed by the direct and reduced order VME models. The displacement in the tensile loading case refers to that prescribed at the boundary, whereas in the shear loading case is the displacement of the top right corner (in both vertical and horizontal directions each of which has the same magnitude and rate as stated above). At the end of the observation period of
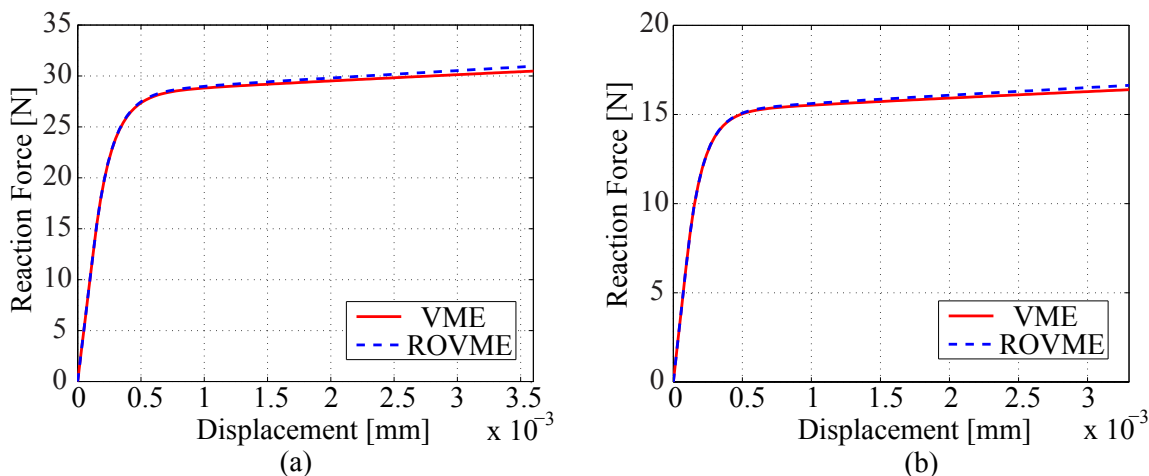
22

Figure 6: Overall reaction force-displacement comparison for the square specimen with circular inclusions between the direct VME simulation and the reduced order VME method: (a) under tension; and (b) under shear.
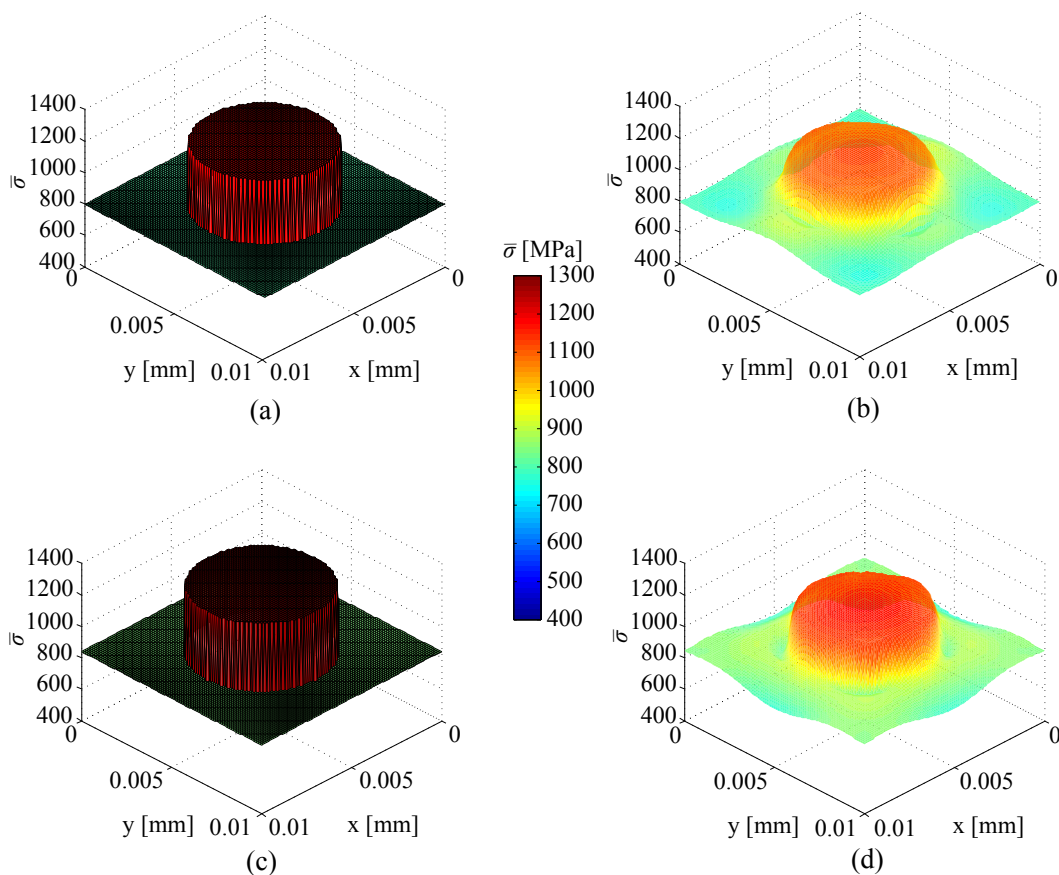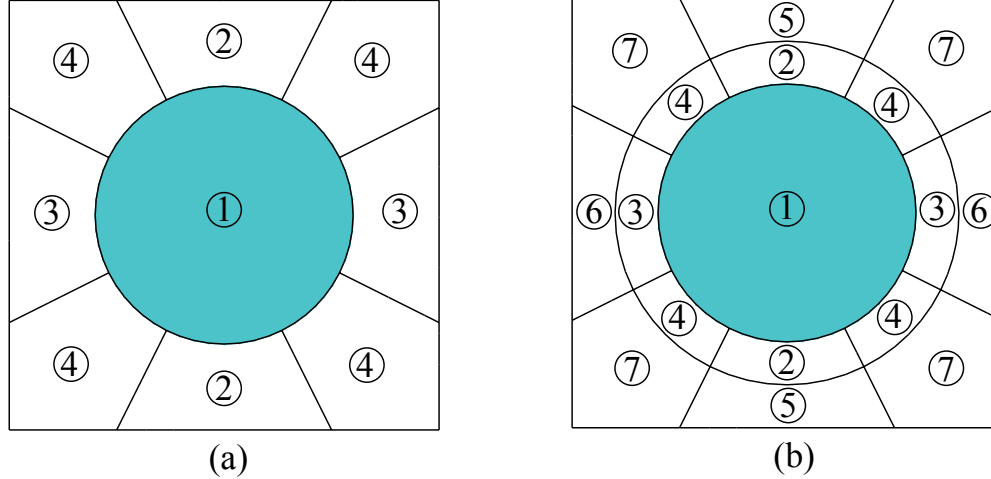

Figure 7: Equivalent stress of the central enrichment domain in the square specimen with circular inclusions: (a) reduced order VME under tension at 432 seconds; (b) direct VME under tension at 432 seconds; (c) reduced order VME under shear at 396 seconds; and (d) direct VME under shear at 396 seconds.

Figure 8: Microscale discretization of an enrichment domain with a circular inclusion: (a) reduced order VME method with 4 parts; and (b) reduced order VME method with 7 parts.

432 seconds, the tensile specimen is under an applied deformation of 3.6×10^{-3} mm. The pure shear case has 3.3×10^{-3} mm applied displacement in both directions and the total simulation time is 396 seconds. The reaction force-displacement plots demonstrate that both models provide near identical behavior, in both elastic and plastic regimes. Figure 7 presents the contour plots of the equivalent stress of the central enrichment domain (the macroscale element at the center of the structure) for both methods, just before failure. The reduced order VME has only two parts in the microscale structure and the stress field is constant on each of the parts. On the other hand, the stress distribution smoothly transitions from stiffer inclusion to the matrix as computed by the direct VME method. The computational cost of the simulations are compared in Table 2 in terms of the total computational time. The computational time for the direct VME simulation is shown in hours [hr], whereas the time for ROVME simulation is presented in minutes [min]. The computational time comparison demonstrates that the reduced order VME approach is much more efficient compared with the direct VME method. We note that the improvement in terms of the computational time is less than the reduction of DOFs.

Table 2: Computational time comparison for square specimen with circular inclusions.

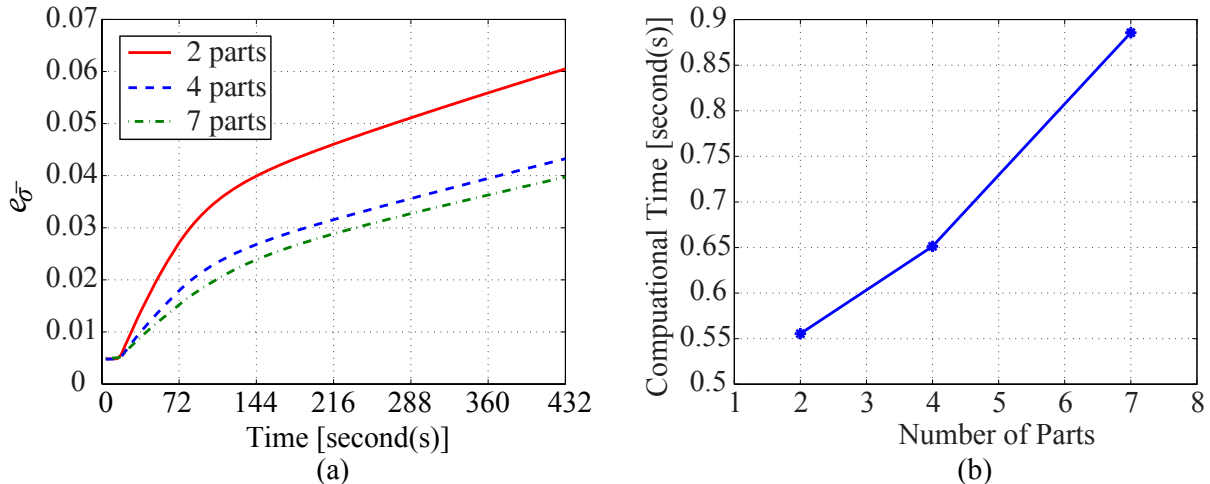| Loading case	Computational time		Computational time ratio	Microscopic DOFs ratio
	VME [hr]	ROVME [min]	VME/ROVME	VME/ROVME
Tension	12.50	11.11	67.53	279
Shear	10.70	11.44	56.08	279

24

Figure 9: Results of reduced order VME method with different parts: (a) error in equivalent stress over the enrichment region as a function of simulation time; and (b) computational time per time step.

To further investigate the computational efficiency of the reduced order VME method, simulations with more parts in the ROVME microscale discretization are performed based on the macroscale model and loading condition shown in Fig. 4(a). In addition to the two-part model as shown in Fig. 5(a), a four-part and a seven-part model as presented in Fig. 8 are considered. The error over the entire enrichment region at an arbitrary time, t, is computed as:

$$e_\phi(t) = \frac{\sum\limits_{\alpha=1}^{n_{\text{en}}} \left\| \phi^{\text{VME}}(\mathbf{x}, t) - \phi^{\text{ROVME}}(\mathbf{x}, t) \right\|_{2,\Omega_\alpha}}{\sum\limits_{\alpha=1}^{n_{\text{en}}} \left\| \phi^{\text{VME}}(\mathbf{x}, t) \right\|_{2,\Omega_\alpha}} \tag{71}$$

where, ϕ^{VME} and ϕ^{ROVME} denote a response field (e.g., equivalent stress) computed using the direct VME method and the reduced order VME method, respectively. $\| \cdot \|_{2,\Omega_\alpha}$ is the L_2 norm of the response field computed over Ω_α. Since all 9 macroscale elements are taken to be enriched in the simulations, the enrichment region is the entire problem domain. For the ROVME method with different parts, the evolution of error in the equivalent stress over the enrichment region as a function of simulation time is compared in Fig. 9(a). The computational time per time step for each simulation is compared in Fig. 9(b). It is observed that the accuracy of the reduced order VME method improves using the model with more parts. But the rate of the accuracy improvement decreases when the number of parts is getting larger, indicating that low order models capture primary response features reasonably well. The computational time increases superlinearly (0.045 second per part from 2 parts to 4 parts and 0.08 second per part from 4 parts to 7 parts). We note that due to small problem size, a substantial time is spent for problem set-up (approximately 82% for the 2-part case).

25

Table 3: Multiple Young's modulus contrasts of the two phases in the enrichment domain.

Case number	Young's modulus [GPa]		Young's modulus ratio $(E_{\text{inclusion}}/E_{\text{matrix}})$
	Inclusion	Matrix	
1	100	1	100
2	100	2	50
3	100	10	10
4	100	20	5
5	100	100	1
6	20	100	0.2
7	10	100	0.1
8	2	100	0.02
9	1	100	0.01
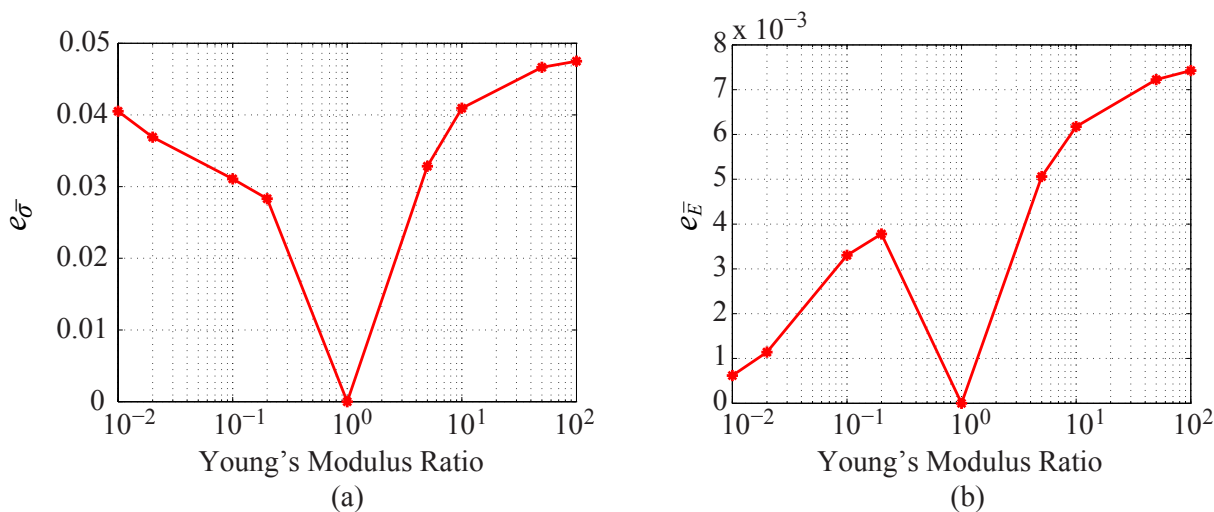
Figure 10: Modulus contrast analysis: (a) error in equivalent stress over enrichment region; and (b) error in the composite stiffness.

26
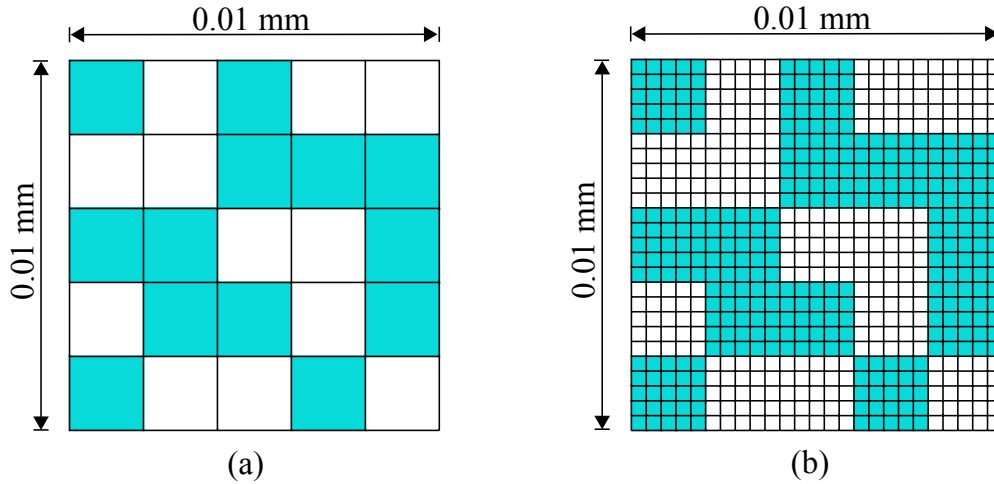
Figure 11: Microscale discretization of an enrichment domain with random grains: (a) reduced order VME method with 25 parts; and (b) direct VME method.

To assess the accuracy of the reduced order VME method for phases with higher modulus contrasts in the enrichment domain, more numerical verifications are performed. The study is conducted under tensile loading (Fig. 4(a)) using the 2-part reduced order VME model (Fig. 5(a)). The elastic behavior of all constituents is assumed in the enrichment domain. Young's modulus contrasts for 9 cases considered are summarized in Table 3. The Poisson's ratio is 0.32 for all the materials. For each case, the error in equivalent stress over the entire enrichment region is computed using Eq. (71). These errors are plotted in Fig. 10(a) as a function of modulus contrast. The composite stiffness, $\bar{E}$, is obtained through the reaction force - displacement plot of each test ($\bar{E}$ = (reaction force / area) / (displacement/ structural length)). The errors in the composite stiffness are plotted in Fig. 10(b), with respect to the modulus contrast. When the modulus ratio is one, the reduced order VME method produces identical results as the direct VME method (error in both plots is zero), due to the fact that there is no material heterogeneity in the enrichment domain (material properties are the same everywhere). As the modulus contrast gets larger, the error in stress rises in a decreasing rate. The same pattern is observed for the error in the composite stiffness. For modulus ratio lower than unity, an increase in composite stiffness error followed by a reduction as a function of modulus contrast is observed. When the inclusion modulus is small, the stiffness is dominated by the matrix properties only, which is well-captured by the reduced order VME approach.

5.2   Square specimen with random grains

A second set of numerical simulations is performed to study the accuracy of the proposed approach in capturing the local microstructural response characteristics. The microstructure contains 25 randomly placed square grains with two material phases, phase I (dark) and phase
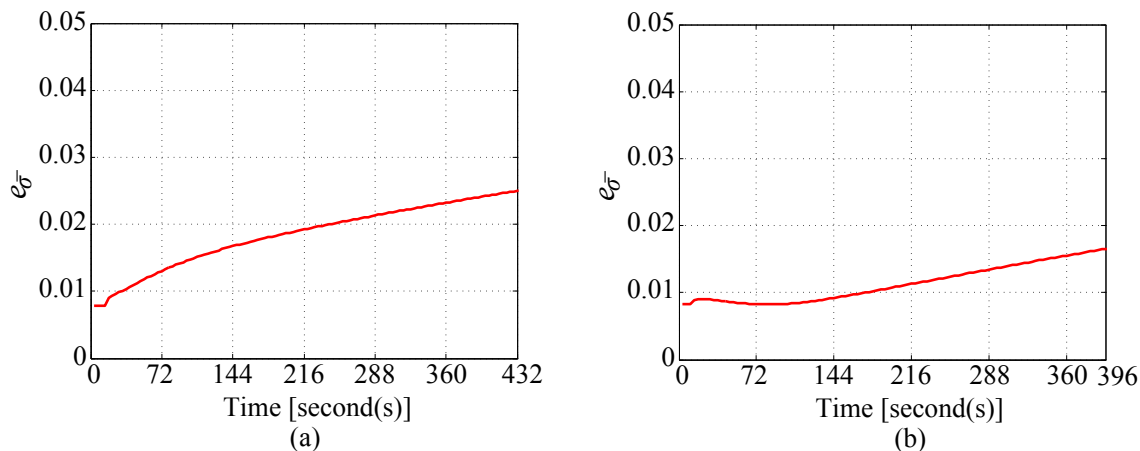
27

Figure 12: Error in equivalent stress over the enrichment region as a function of simulation time for the square specimen with random grains: (a) under tension; and (b) under shear.

II (light), as illustrated in Fig. 11. In reduced order model partitioning, each grain is taken as a part. The direct VME method further discretizes each grain with 25 finite elements. The ROVME microscale partitioning has 25 parts and 75 DOFs whereas the direct VME microscale grid contains 625 quadrilateral finite elements with 676 nodes and 1352 DOFs. Identical macroscale discretization and loading conditions of the specimen as shown in Fig. 4 are used in the current example. The loading rate, time step size and observation periods for both loading cases are the same as those in Section 5.1.

Identical to the previous numerical examples, the enrichment region is the entire problem domain which includes all of the 9 macroscale elements. The evolution of error in the equivalent stress over the enrichment region as a function of simulation time is shown in Fig. 12 for both tensile and shear loading conditions. At an arbitrary time step, the error is evaluated using Eq. (71). It can be observed that the error in stress slightly accumulates along with the increase in plastic strain. The maximum error is at the end of the simulation where failure is set to initiate. The increase in error in time is consistent with the example in Section 5.1, due to the slightly larger hardening modulus predicted by the reduced order model. For the shear loading case, the error in stress slightly decreases shortly after entering the plastic regime due to the stress redistribution within the enrichment region which softens the rigid kinematics of the reduced order model. The error starts to accumulate once the stress redistribution is completed. At the onset of failure initiation within the structure, the highest error in equivalent stress is 2.5% for the tensile loading and 1.7% for the shear loading, as shown in Fig. 12. The local equivalent stress contours for the central enrichment domain, corresponding to the prescribed peak load at the end of the simulations, are shown in Fig. 13. The stress contours demonstrate that the reduced order VME method captures the local stress variation
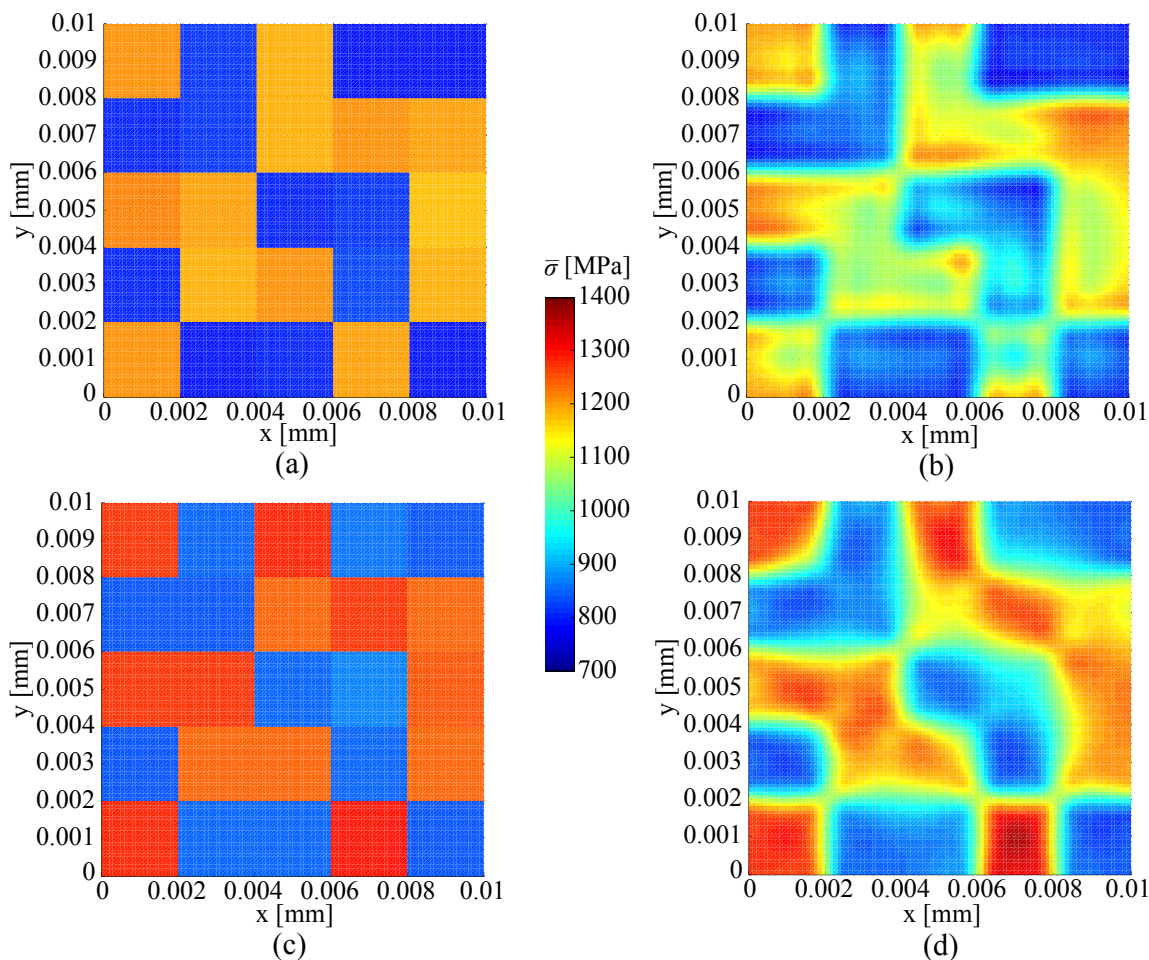
28

Figure 13: Equivalent stress contour of the central enrichment domain in the specimen with random grains: (a) reduced order VME under tension at 432 seconds; (b) direct VME under tension at 432 seconds; (c) reduced order VME under shear at 396 seconds; and (d) direct VME under shear at 396 seconds.

within the microstructure reasonably well (0.8% - 2.5% error). The overall reaction force vs. prescribed displacement comparison is presented in Fig. 14. The figure shows that the global behavior of the reduced order VME method closely agrees with the direct VME method, in both elastic and plastic states. The comparisons of the global and local responses verified the high accuracy of the reduced order VME method, even using relatively coarse microscale partitioning. The computational time of both simulations are listed and compared in Table 4. The reduced order VME reduces the computational effort of the direct VME method by at least the same reduction in DOFs, which points to very favorable computational cost of the proposed approach.
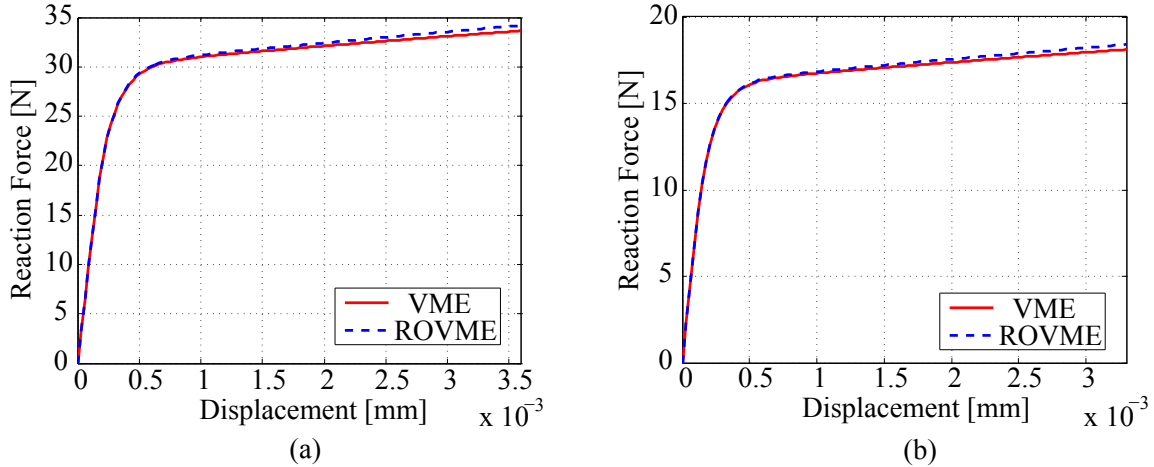
Figure 14: Overall reaction force-displacement comparison for the square specimen with particles between the direct VME simulation and the reduced order VME method: (a) under tension; and (b) under shear.

Table 4: Computational time comparison for square specimen with particles.

Loading case	Computational time		Computational time ratio	Microscopic DOFs ratio
	VME [hr]	ROVME [min]	VME/ROVME	VME/ROVME
Tensile	13.69	15.81	51.94	18.03
Shear	4.75	15.94	17.89	18.03

5.3 L-shaped specimen with random grains

The proposed ROVME method is further verified using the numerical analysis of an L-shaped specimen which contains both enrichment and substrate regions while subjected to more complex stress states. The geometry, loading condition and the macroscale discretization are illustrated in Fig. 15. The enrichment region (identified with dark shading) is placed within the area of stress concentration, around the inner corner of the specimen. The characteristic size scale ratio defined as the ratio between the size of the enrichment domain and the length scale associated with high stress gradients around the corner is approximately 1/6. The macroscale mesh consists of 192 quadrilateral elements, 27 of which are enriched. Within the enrichment domains of the enrichment region, the microstructural geometry for reduced order model partitioning and for the direct discretization are identical to those shown in Fig. 11. The material properties of the phases, as well as within the substrate region, are summarized in Table 1. The specimen is subjected to uniform displacement controlled loading in the vertical direction along the right edge of the specimen as shown in Fig. 15. The maximum amplitude of the loading is 0.0256 mm applied in 576 seconds, at a rate of 4.4×10^{-5} mm/sec, which corresponds to the onset of failure initiation within the specimen. Further loading would lead
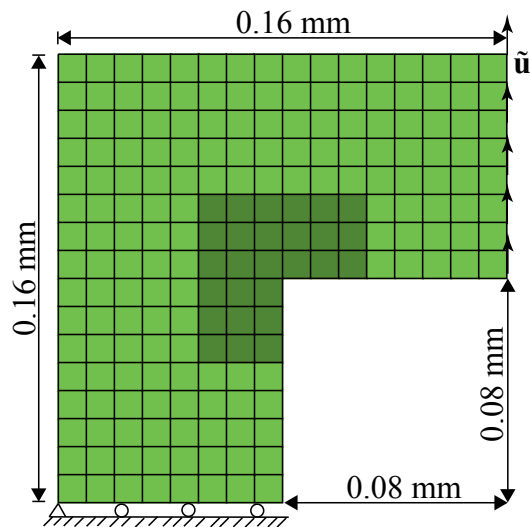
30

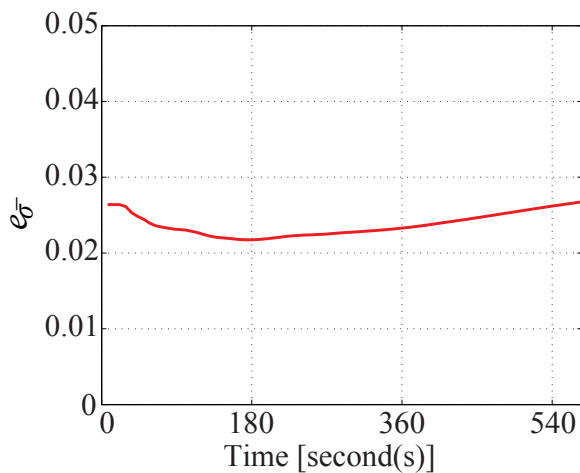Figure 15: Macroscale discretization and sketch for L-shaped specimen.

Figure 16: Error in equivalent stress as a function of time for the L-shaped specimen.

to failure within the structure. The simulation time step size is set to be 0.72 second and the convergence tolerance is taken to be 1×10^{-3} which is the same as employed in Sections 5.1 and 5.2 .

Figure 16 illustrates the evolution of error in equivalent stress within the enrichment region, which is plotted as a function of simulation time. The errors at each time step is computed using Eq. (71). The maximum error in the stress is less than 2.7% which further substantiates the accuracy characteristics of the proposed reduced order VME methodology. The error in stress slightly decreases after the onset of the plastic deformation, due to the stress redistribution over the enrichment region which softens the rigid kinematics of the reduced order model. The error increases thereafter and reaches the maximum value at the end of the simulation, similar to the previous example. Figure 17 presents the comparison of the overall force -
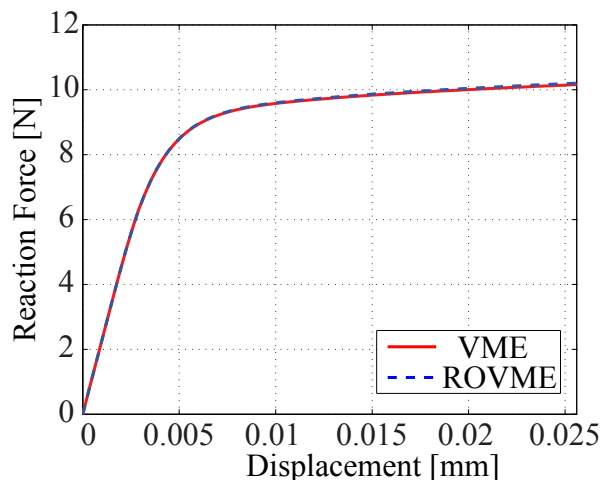
31

Figure 17: L-shaped specimen overall reaction force-displacement comparison between the direct VME simulation and the reduced order VME method.

displacement curves from the direct VME method and the reduced order VME simulation. The close agreement of the two model predictions demonstrates that the proposed reduced order approach accurately captures the global elasto-viscoplastic response of the structure. The equivalent stress contours at the end of the simulations are presented for both of the approaches in Fig. 18. For both approaches, the stress contours are obtained by combining the fine and coarse scale responses and reconstructing the total stress in the post-processing phase. Since the resolution of the reduced order VME method is much lower than the direct VME method, the stress contour of the reduced order VME method is slightly smoother than the direct VME method. The stress variation of the ROVME simulation within the domain closely approximates that predicted by the reference model. The computational cost of the simulations are presented in Table 5, which clearly shows the computational benefits of the reduced order VME methodology.

Table 5: Computational time comparison for L-shaped specimen.

Computational time		Computational time ratio	Microscopic DOFs ratio
VME [hr]	ROVME [min]	VME/ROVME	VME/ROVME
66.66	31.14	128.44	18.03

6   Conclusions and Future Research

This manuscript presented a novel reduced order variational multiscale enrichment method for elasto-viscoplastic problems. The proposed ROVME approach allows reduced order microscale
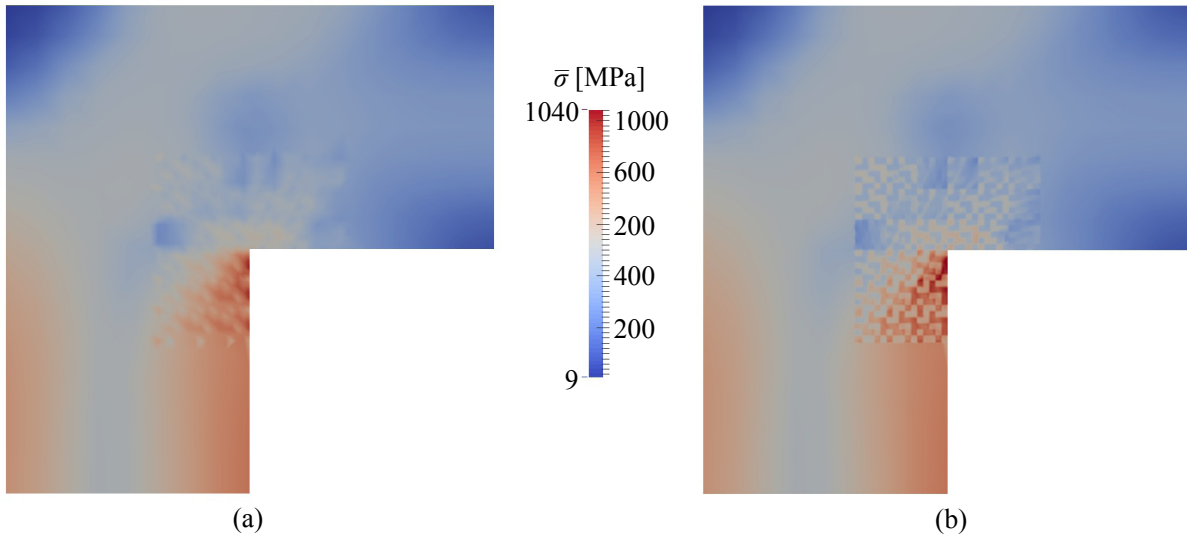
Figure 18: Equivalent stress contours of the L-shaped specimen with random grains at 576 seconds: (a) reduced order VME model; (b) direct VME model.

representation at critical subdomains while maintaining most of the accuracy of the direct VME method. This approach extends the eigenstrain-based reduced order modeling [43] to scale inseparable problems. With coarse stress and inelastic strain fields discretization within the microscale domain, the proposed formulation automatically satisfies the microscale equilibrium state. The performance of the proposed computational framework is assessed against direct variational multiscale enrichment method with full microscale discretization. It is verified that the reduced order VME method accurately captures the local response within the subdomains of interest, as well as the global behavior of the structure.

To expand the applicability of the proposed computational framework, particularly to structures operating in severe environments, several issues remain to be resolved. In order to address structural response subject to mechanical loads in aggressive environments, aggressive agent diffusion and coupling effect should be incorporated into the current computational framework and evaluated in conjunction with the mechanical problems. For example, many coupling mechanisms of aggressive agent diffusion in structures operating in high temperature environment has been identified in Refs. [44, 49, 50]. The temperature-dependent material behavior should also be considered in problems involving thermal transients or high temperatures. Moreover, the incorporation of failure response is critical to the prediction of structural life. In its current state, the proposed reduced order VME approach has the ability to accurately predict failure initiation. The challenge remaining is the accurate failure propagation prediction. Other important issues, such as the automated determination of the size of the enrichment region (as well as the enrichment domains) and the analysis of the response subject to cyclic loading, would also extend the applicability of the proposed method. The issues

mentioned above will be investigated in the near future.

7   Acknowledgements

References

[1] *Department of Defense Handbook - Metallic material and elements for aerospace vechicle structures, MIL-HDBK-5J, 2003.*

[2] T. Arbogast. Implementation of a locally conservative numerical subgrid upscaling scheme for two-phase Darcy flow. *Comput. GeoSci.*, 6:453–481, 2002.

[3] T. Arbogast. Analysis of a two-scale, locally conservative subgrid upscaling for elliptic problems. *SIAM J. on Numer. Anal.*, 42:576–598, 2004.

[4] I. Babuska. *Homogenization and application: mathematical and computational problems, in: B. Hubbard (Ed.), Numerical Solution of Partial Differential Equations - III.* SYNSPADE, Academic Press, New York, 1975.

[5] T. Belytschko, S. Loehnert, and J. Song. Multiscale aggregating discontinuities: A method for circumventing loss of material stability. *Int. J. Numer. Meth. Engng.*, 73:869–894, 2008.

[6] F. Brezzi, L. P. Franca, T. J. R. Hughes, and A. Russo. $b = \int g$. *Comput. Methods Appl. Mech. Engrg.*, 145:329–339, 1997.

[7] R. Courant and D. Hilbert. *Methods of Mathematical Physics, Volume 1.* Wily-VCH, 1991.

[8] R. Crouch and C. Oskay. Symmetric meso-mechanical model for failure analysis of heterogeneous materials. *Int. J. Solids Struct.*, 8:447–461, 2010.

[9] C. A. Duarte and D. J. Kim. Analysis and applications of a generalized finite element method with global–local enrichment functions. *Comput. Methods Appl. Mech. Engrg.*, 197:487–504, 2008.

[10] G.J. Dvorak and Y. Benveniste. On transformation strains and uniform fields in multi-phase elastic media. *Proc. R. Soc. Lond. A*, 437:291–310, 1992.

[11] Y. Efendiev and T. Y. Hou. *Multiscale Finite Element Methods-Theory and Applications*. Springer-Verlag, New York, 2009.

[12] J. Fish. The s-version of the finite element method. *Computers & Structures*, 43:539–547, 1992.

[13] J. Fish and S. Markolefas. Adaptive global-local refinement strategy based on the interior error estimates of the h-method. *Int. J. Numer. Meth. Engng.*, 37:827–838, 1994.

[14] J. Fish, K. Shek, M. Pandheeradi, and M. Shephard. Computational plasticity for composite structures based on mathematical homogenization: Theory and practice. *Comput. Methods Appl. Mech. Engrg.*, 148:53–73, 1997.

[15] K. Garikipati and T. J. R. Hughes. A study of strain localization in a multiple scale framework: The one-dimensional problem. *Comput. Methods Appl. Mech. Engrg.*, 159: 193–222, 1998.

[16] K. Garikipati and T. J. R. Hughes. A variational multiscale approach to strain localization formulation for multidimensional problems. *Comput. Methods Appl. Mech. Engrg.*, 188: 39–60, 2000.

[17] M. G. D Geers, V. Kouznetsova, and W. A. M. Brekelmans. Gradient-enhanced computational homogenization for the micro-macroscale transition. *J. Phys. IV*, 11:145–152, 2001.

[18] L. Gendre, O. Allix, P. Gosselet, and F. Comte. Non-intrusive and exact global/local techniques for structural problems with local plasticity. *Comput. Mech.*, 44:233–245, 2009.

[19] S. Ghosh, K. Lee, and S. Moorthy. Two scale analysis of heterogeneous elastic-plastic materials with asymptotic homogenization and voronoi cell finite element model. *Comput. Methods Appl. Mech. Engrg.*, 132:63–116, 1996.

[20] J. M. Guedes and N. Kikuchi. Preprocessing and postprocessing for materials based on the homogenization method with adaptive finite element methods. *Comput. Methods Appl. Mech. Engrg.*, 83:143–198, 1990.

[21] V. Guptaa, C.A. Duartea, I. Babuska, and U. Banerjee. Stable GFEM(SGFEM): Improved conditioning and accuracy of GFEM/XFEM for three-dimensional fracture mechanics. *Comput. Methods Appl. Mech. Engrg.*, 289:355–386, 2015.

[22] T. Y. Hou and X. Wu. A multiscale finite element method for elliptic problems in composite materials and porous media. *J. Comput. Phys.*, 134:169–189, 1997.

[23] T. J. R. Hughes. Multiscale phenomena: Green's functions, the Dirichlet-to-Neumann formulation, subgrid scale models, bubbles and the origins of stabilized methods. *Comput. Methods Appl. Mech. Engrg.*, 127:387–401, 1995.

[24] T. J. R. Hughes and G. Sangalli. Variational multiscale analysis: the fine-scale Green's function, projection, optimization, localization, and stabilized methods. *SIAM J. Numer. Anal.*, 45:539–557, 2007.

[25] T. J. R. Hughes, G. R. Feijoo, and J. B. Quincy. The variational multiscale method - a paradigm for computational mechanics. *Comput. Methods Appl. Mech. Engrg.*, 166:3–24, 1998.

[26] A. Hund and E. Ramm. Locality constraints within multiscale model for non-linear material behaviour. *Int. J. Numer. Meth. Engng.*, 70:1613–1632, 2007.

[27] R. Juanes and F.-X. Dub. A locally conservative variational multiscale method for the simulation of porous media flow with multiscale source terms. *Comput. Geosci.*, 12:273–295, 2008.

[28] V.G. Kouznetsova, M.G.D. Geers, and W.A.M. Brekelmans. Multi-scale second-order computational homogenization of multi-phase materials: a nested finite element solution strategy. *Comput. Methods Appl. Mech. Engrg.*, 193:5525–5550, 2004.

[29] H. P. Langtangen. *Computational partial differential equations: Numerical methods and diffpack programming.* Springer, 2003.

[30] O. Lloberas-Valls, D. J. Rixen, A. Simone, and L. J. Sluys. Domain decomposition techniques for the efficient modeling of brittle heterogeneous materials. *Comput. Methods Appl. Mech. Engrg.*, 200:1577–1590, 2011.

[31] K. M. Mao and C. T. Sun. A refined global-local finite element analysis method. *Int. J. Numer. Meth. Engng.*, 32:29–43, 1991.

[32] D. Markovic and A. Ibrahimbegovic. On micro-macro interface conditions for micro scale based FEM for inelastic behavior of heterogeneous materials. *Comput. Methods Appl. Mech. Engrg.*, 193:5503–5523, 2004.

[33] A. Masud and K. Xia. A variational multiscale method for inelasticity: Application to superelasticity in shape memory alloys. *Comput. Methods Appl. Mech. Engrg.*, 195: 4512–4531, 2006.

[34] A. Masud, T. J. Truster, and L. A. Bergman. A variational multiscale a posteriori error estimation method for mixed form of nearly incompressible elasticity. *Comput. Methods Appl. Mech. Engrg.*, 200:3453-3481, 2011.

[35] K. Matous, H.M. Inglis, X. Gu, D. Rypl, T.L. Jackson, and P.H. Geubelle. Multiscale modeling of solid propellants: From particle packing to failure. *Compos. Sci. Technol.*, 67:1694–1708, 2007.

[36] J. C. Michel and P. Suquet. Nonuniform transformation field analysis. *Int. J. Solids Struct.*, 40:6937–6955, 2003.

[37] J.C. Michel and P. Suquet. Computational analysis of nonlinear composite structures using the nonuniform transformation field analysis. *Comput. Methods Appl. Mech. Engrg.*, 193:5477–5502, 2004.

[38] C. D. Mote. Global-local finite element. *Int. J. Numer. Meth. Engng.*, 3:565–574, 1971.

[39] H. Moulinec and P. Suquet. A numerical method for computing the overall response of nonlinear composites with complex microstructure. *Comput. Methods Appl. Mech. Engrg.*, 157:69–94, 1998.

[40] A. K. Noor. Global-local methodologies and their application to nonlinear analysis. *Finite Elements Anal. Des.*, 2:333–346, 1986.

[41] C. Oskay. Variational multiscale enrichment for modeling coupled mechano-diffusion problems. *Int. J. Numer. Meth. Engng.*, 89:686–705, 2012.

[42] C. Oskay. Variational multiscale enrichment method with mixed boundary conditions for modeling diffusion and deformation problems. *Comput. Methods Appl. Mech. Engrg.*, 264: 178–190, 2013.

[43] C. Oskay and J. Fish. Eigendeformation-based reduced order homogenization for failure analysis of heterogeneous materials. *Comput. Methods Appl. Mech. Engrg.*, 196:1216–1243, 2007.

[44] C. Oskay and M. Haney. Computational modeling of titanium structures subjected to thermo-chemo-mechanical environment. *Int. J. Solids Struct.*, 47:3341–3351, 2010.

[45] P. Ponte Castaneda. The effective mechanical properties of nonlinear isotropic composites. *J. Mech. Phys. Solids*, 39:45–71, 1991.

[46] S. Roussette, J.C. Michel, and P. Suquet. Nonuniform transformation field analysis of elastic-viscoplastic composites. *Compos. Sci. Technol.*, 69:22–27, 2009.

[47] J. Song and T. Belytschko. Multiscale aggregating discontinuities method for micro-macro failure of composites. *Composites: Part B*, 40:417–426, 2009.

[48] K. Terada and M. Kurumatani. Two-scale diffusion-deformation coupling model for material deterioration involving micro-crack propagation. *Int. J. Numer. Meth. Engng*, 83: 426–451, 2010.

[49] H. Yan and C. Oskay. A three-field (displacement-pressure-concentration) formulation for coupled transport-deformation problems. *Finite Elements Anal. Des.*, 90:20–30, 2014.

[50] H. Yan and C. Oskay. A viscoelastic-viscoplastic model of titanium structures subjected to thermo-chemo-mechanical environment. *Int. J. Solids Struct.*, 56-57:29–42, 2015.

[51] S. Zhang and C. Oskay. Variational multiscale enrichment method with mixed boundary conditions for elasto-viscoplastic problems. *Comput. Mech.*, 55:771–787, 2015.

[52] X. Zhang and C. Oskay. Eigenstrain based reduced order homogenization for polycrystalline materials. *Comput. Methods Appl. Mech. Engrg.*, 2015. DOI: 10.1016/j.cma.2015.09.006

A   Computation of C and G matrices

This appendix section presents the details of $\mathbf{C}_\gamma^\alpha = \left(\frac{\partial \dot{\boldsymbol{\mu}}_\gamma^\alpha}{\partial \boldsymbol{\sigma}_\gamma^\alpha}\right)$ and $\mathbf{G}_\gamma^\alpha = \left(\frac{\partial \dot{\boldsymbol{\mu}}_\gamma^\alpha}{\partial \boldsymbol{\mu}_\gamma^\alpha}\right)$ that are illustrated in Section 4.1. This section provides the formulation for 3D case which can be simplified to 2D case, such as plane stress or plane strain problem, based on the problem nature. For the clarity of presentation, the bold symbol in this section denotes vector notation. Recall the evolution of plastic strain (Eq. (14)), the loading function (Eq. (15)) and the flow stress (Eq. (17)). Define

$$F \equiv \frac{f(\boldsymbol{\sigma}_\gamma^\alpha, \boldsymbol{\mu}_\gamma^\alpha)}{\sigma_y(\boldsymbol{\mu}_\gamma^\alpha)} \tag{72}$$

and

$$\mathbf{a} \equiv \frac{\partial f(\boldsymbol{\sigma}_\gamma^\alpha, \boldsymbol{\mu}_\gamma^\alpha)}{\partial \boldsymbol{\sigma}_\gamma^\alpha} = \sqrt{3}\frac{\partial \bar{\sigma}_\gamma^\alpha}{\partial \boldsymbol{\sigma}_\gamma^\alpha} = \frac{\sqrt{3}}{2\bar{\sigma}_\gamma^\alpha}\tilde{\boldsymbol{\sigma}}_\gamma^\alpha \tag{73}$$

where, in 3D case $\tilde{\boldsymbol{\sigma}}_\gamma^\alpha$ is expressed in a vector format as:

$$\tilde{\boldsymbol{\sigma}}_\gamma^\alpha = \left\{ s_\gamma^\alpha(xx), s_\gamma^\alpha(yy), s_\gamma^\alpha(zz), 2\sigma_\gamma^\alpha(xy), 2\sigma_\gamma^\alpha(yz), 2\sigma_\gamma^\alpha(zx) \right\}^T \tag{74}$$

in which s denotes deviatoric stress components. Consequently, the inelastic coefficient evolution equation is expressed as:

$$\dot{\boldsymbol{\mu}}_\gamma^\alpha = \gamma \langle F \rangle^q \mathbf{a} \tag{75}$$

and $\mathbf{C}_\gamma^{\alpha,k}$ becomes:

$$\begin{aligned}\mathbf{C}_\gamma^\alpha = \left(\frac{\partial \dot{\boldsymbol{\mu}}_\gamma^\alpha}{\partial \boldsymbol{\sigma}_\gamma^\alpha}\right) &= \gamma \left[\langle F \rangle^q \frac{\partial \mathbf{a}}{\partial \boldsymbol{\sigma}} + q\langle F \rangle^{q-1} \frac{\partial \langle F \rangle}{\partial f}\frac{\partial f}{\partial \boldsymbol{\sigma}} \otimes \mathbf{a} \right] \\ &= \gamma \langle F \rangle^q \left[\frac{\partial \mathbf{a}}{\partial \boldsymbol{\sigma}} + \frac{q[\text{sign}(F)+1]}{2\langle f \rangle}\mathbf{a} \otimes \mathbf{a} \right]\end{aligned} \tag{76}$$

The derivative of Eq. (73) with respect to the stress coefficient is obtained as:

$$\frac{\partial \mathbf{a}}{\partial \boldsymbol{\sigma}_\gamma^\alpha} = \frac{\sqrt{3}}{2\bar{\sigma}_\gamma^\alpha}\mathbf{M} - \frac{\sqrt{3}}{3\bar{\sigma}_\gamma^\alpha}\mathbf{a} \otimes \mathbf{a}; \quad \mathbf{M} = \frac{\partial \tilde{\boldsymbol{\sigma}}_\gamma^\alpha}{\partial \boldsymbol{\sigma}_\gamma^\alpha} \tag{77}$$

In 3D case, $\mathbf{M}$ is expressed as:

$$\mathbf{M} = \begin{bmatrix} \frac{2}{3} & -\frac{1}{3} & -\frac{1}{3} & 0 & 0 & 0 \\ -\frac{1}{3} & \frac{2}{3} & -\frac{1}{3} & 0 & 0 & 0 \\ -\frac{1}{3} & -\frac{1}{3} & \frac{2}{3} & 0 & 0 & 0 \\ 0 & 0 & 0 & 2 & 0 & 0 \\ 0 & 0 & 0 & 0 & 2 & 0 \\ 0 & 0 & 0 & 0 & 0 & 2 \end{bmatrix} \tag{78}$$

Employing $\mathbf{M}$, $\mathbf{C}_\gamma^\alpha$ is expressed as:

$$\mathbf{C}_\gamma^\alpha = \gamma \langle F \rangle^q \left[\frac{\sqrt{3}}{2\bar{\sigma}_\gamma^\alpha} \mathbf{M} + \left(\frac{q \left[\mathrm{sign}(F) + 1 \right]}{2 \langle f \rangle} - \frac{\sqrt{3}}{3\bar{\sigma}_\gamma^\alpha} \right) \mathbf{a} \otimes \mathbf{a} \right] \tag{79}$$

Taking derivative of Eq. (75) with respect to inelastic strain coefficient, $\mathbf{G}_\gamma^\alpha$ yields:

$$\mathbf{G}_\gamma^\alpha = \frac{\partial \dot{\boldsymbol{\mu}}_\gamma^\alpha}{\partial \boldsymbol{\mu}_\gamma^\alpha} = \frac{\gamma \ q}{2} \langle F \rangle^{q-1} \left[\mathrm{sign}(F) + 1 \right] \frac{\partial F}{\partial \boldsymbol{\mu}_\gamma^\alpha} \otimes \mathbf{a} \tag{80}$$

Through chain rule, the derivative of Eq. (72) with respect to inelastic strain coefficient is obtained as:

$$\frac{\partial F}{\partial \boldsymbol{\mu}_\gamma^\alpha} = \frac{\partial f}{\partial \bar{\mu}_\gamma^\alpha} \frac{\partial \bar{\mu}_\gamma^\alpha}{\partial \boldsymbol{\mu}_\gamma^\alpha} \frac{1}{\sigma_y} - \frac{f}{\sigma_y{}^2} \frac{\partial \sigma_y}{\partial \bar{\mu}_\gamma^\alpha} \frac{\partial \bar{\mu}_\gamma^\alpha}{\partial \boldsymbol{\mu}_\gamma^\alpha} = -\frac{2}{3} Bn(\bar{\mu}_\gamma^\alpha)^{n-2} \left(\frac{\sigma_y + f}{\sigma_y{}^2} \right) \boldsymbol{\mu}_\gamma^\alpha \tag{81}$$

Substituting Eq. (81) into Eq. (80) yields:

$$\mathbf{G}_\gamma^\alpha = -[\mathrm{sign}(F) + 1] \left(\frac{\gamma \ q \ B \ n}{3} \right) \langle F \rangle^{q-1} \ (\bar{\mu}_\gamma^\alpha)^{n-2} \ \left(\frac{\sqrt{3}\bar{\sigma}_\gamma^\alpha}{\sigma_y{}^2} \right) \boldsymbol{\mu}_\gamma^\alpha \otimes \mathbf{a} \tag{82}$$

40